atmosphere

MDPI

Article

Estimating Local Air Pollutant Contribution Ratio Based on Concentration Variability Among Monitoring Stations

Yixuan Wang [1], Jianghui Liu [1], Qiaoyu Ma [1], Xinxin Yang [1], Yadong Wang [1], Ying Zhou [1] and Jianlei Lang [1,2,*]

[1] Key Laboratory of Beijing on Regional Air Pollution Control, College of Environmental Science and Engineering, Beijing University of Technology, Beijing 100124, China
[2] Beijing Laboratory for Intelligent Environmental Protection, Beijing University of Technology, Beijing 100124, China
* Correspondence: jllang@bjut.edu.cn

Abstract

Quantifying the relative contributions of local emissions and regional transport is critical for urban air quality management. Chemical transport models (CTMs) are widely applied for source apportionment, but they require detailed emission inventories, extensive input data, and substantial computational resources, which limit their operational use. In contrast, urban monitoring networks provide continuous and readily available observations. This study develops an observation-based framework that estimates regional contribution ratios (RCs) from inter-station concentration variability, quantified by the coefficient of variation (CV), using WRF–CAMx results as a reference. Using Linyi as the primary case, with Xi'an and Beijing for comparison, concentration-stratified regression was applied to establish CV–RC relationships. Results show a consistent nonlinear relationship between CV and RC, with coefficients of determination (R^2) up to 0.86 for PM_{10} (daily), 0.81 for NO_2 (hourly), and 0.78–0.79 for O_3. CV decreases markedly with increasing concentration; for $PM_{2.5}$, values decline from ~0.17–0.18 to 0.05–0.06 (≈65–70%), indicating enhanced spatial homogeneity under regional influence. The relationship is most stable within a 10–15 km spatial scale. Application-based evaluation for January 2022 shows moderate agreement between estimated and modeled RC (R = 0.55–0.65), reflecting pollutant-dependent uncertainties, partly associated with biases in the model-derived reference RC. These results demonstrate that inter-station concentration variability provides a first-order, computationally efficient indicator of the balance between local emissions and regional transport.

Keywords: local contribution estimation; atmospheric transport processes; WRF-CAMx; concentration variability; monitoring stations

Received: 9 March 2026
Revised: 4 May 2026
Accepted: 5 May 2026
Published: 8 May 2026

1. Introduction

Rapid urbanization has led to sustained growth in anthropogenic emissions, making air pollution a persistent problem in many regions. Urban areas concentrate both emission sources and population exposure, resulting in substantial public health impacts [1–3]. However, urban air quality is not determined solely by local emissions. Pollutant concentrations typically result from the interplay among local emission intensity, atmospheric dispersion conditions, and regional transport processes [4–6]. Effective control strategies require clear identification of whether pollution episodes are dominated by local emissions or by regional transport processes [7]. Quantifying their relative contributions provides a scientific basis for emission reduction planning, policy evaluation, and coordinated regional control actions [8–10].

Chemical transport models are widely used to estimate local and regional contributions [11]. Modeling systems such as WRF–CAMx [11,12], CMAQ [13,14], and WRF–Chem [15,16] can track source-region impacts under different meteorological conditions and have been extensively applied to investigate ozone and particulate matter formation and source apportionment. However, model-based approaches strongly depend on emission inventories [17,18], chemical mechanisms [19], boundary conditions [20], and substantial computational resources. Their implementation requires technical expertise and high computing capacity, which may limit rapid or routine estimation in many cities [21]. In addition, uncertainties in emissions and parameterizations can influence contribution estimates [22].

In addition to CTM-based approaches, a range of observation-based and data-driven methods have been developed to interpret source influences in urban environments. Receptor-oriented models such as Positive Matrix Factorization (PMF) and Chemical Mass Balance (CMB) infer source contributions from chemical composition data and remain important tools in source apportionment. Yet they typically require speciated measurements, while CMB additionally relies on representative source profiles; moreover, they do not directly characterize the time-varying local–regional balance across a monitoring network without additional transport-based or trajectory-based analysis [23–26]. Other studies have utilized empirical and statistical analyses of monitoring networks, including spatial coherence metrics and inter-station representativeness, to characterize pollution structures and infer the relative roles of regional transport and local influences [27–31]. These approaches exploit spatial correlations and variability across sites to diagnose transport pathways and source influences. However, these methods either rely on speciated measurements, predefined source profiles, or do not directly provide a rapid and interpretable indicator of local–regional contribution balance across monitoring networks. More recently, machine learning and data-driven frameworks have been explored for source attribution, offering computational efficiency but often with reduced physical interpretability [32–34].

At the same time, urban monitoring networks have accumulated large amounts of high frequency observational data [35]. These data contain implicit information about spatial relationships among stations and about the balance between local emission heterogeneity and regional atmospheric mixing [36,37]. When regional transport dominates, air masses may become more spatially homogeneous across an urban area, and concentration differences among monitoring stations may decrease [38]. In contrast, when local emissions dominate under weak ventilation conditions, spatial heterogeneity across stations may increase [39,40]. This physical contrast suggests that inter-station concentration variability may serve as an empirical indicator of the balance between local emission heterogeneity and regional transport. Such information is directly relevant for practical air quality management, as it may help identify whether pollution conditions are locally dominated or influenced by regional transport, thereby supporting decisions on the relative importance of local emission control versus coordinated regional mitigation strategies. In this context, the coefficient of variation (CV) provides a normalized measure of relative spatial heterogeneity among monitoring stations.

To further support this physical interpretation, previous studies have extensively examined intra-urban air quality variability and inter-station differences, primarily focusing on how such spatial heterogeneity can be quantified, interpreted, and applied in monitoring network analysis. A substantial body of work has demonstrated that pollutant concentrations can vary significantly within cities due to differences in emission sources, urban morphology, and atmospheric conditions. For instance, comprehensive reviews have highlighted that intra-urban variability in particulate matter is a well-established phenomenon with important implications for exposure assessment and epidemiological

studies [41]. Methodological studies further confirm that within-urban variability is a key challenge in air pollution modeling and assessment, with substantial differences observed across monitoring sites depending on spatial scale and estimation approach [42]. In addition, observational and source apportionment analyses have shown that not only pollutant concentrations but also source contributions can exhibit strong spatial heterogeneity within a single airshed [43].

To quantify such spatial heterogeneity, statistical indicators such as the CV, coefficient of divergence (COD), and correlation-based metrics have been widely applied in air quality studies. These indicators have been used to characterize inter-station variability and assess the spatial representativeness of monitoring networks. For example, Martuzevicius et al. quantified the spatial variability of $PM_{2.5}$ concentrations across an urban monitoring network using a spatial CV [44], while Faridi et al. employed CV in combination with COD to evaluate the spatial homogeneity and heterogeneity of multiple air pollutants across monitoring stations [45]. These studies demonstrate that CV and related metrics are effective tools for describing spatial differences in pollutant concentrations.

Previous studies have also provided empirical evidence supporting these mechanisms. For example, Wu et al. showed that the spatial variability of different particulate matter components is governed by distinct drivers, with traffic emissions, street-scale morphology, and synoptic meteorological conditions playing different roles [46]. Similarly, Kim et al. found that spatial differences in $PM_{2.5}$ are closely linked to variations in source contributions [43]. In addition, Barrero et al. showed that pollutant variability is directly related to emission patterns and dispersion dynamics [47].

Despite these advances, previous studies have primarily treated inter-station variability as a descriptive indicator of spatial heterogeneity or a tool for monitoring network evaluation. They have rarely developed such variability metrics into an observation-based indicator for quantitatively diagnosing the relative contributions of local emissions versus regional transport. More importantly, it remains unclear whether and under what conditions inter-station variability can be translated into a robust, scale-aware, and observation-based estimate of local–regional contribution. To address this gap, the present study establishes a direct and quantitative linkage between inter-station variability (CV) and regional contribution (RC) through a concentration-stratified and scale-dependent mapping framework. Rather than introducing CV as a new statistical metric, this study redefines its role from a descriptive measure of variability to a physically interpretable and observation-based indicator of emission–transport dynamics.

In this study, we develop a rapid, observation-based estimation framework that links monitoring-derived concentration variability to regional contribution ratios through a concentration-stratified and scale-dependent mapping approach. Inter-station variability is quantified using the CV, which serves as a normalized indicator of spatial heterogeneity among monitoring stations. We emphasize that while CV has been widely used as a descriptive metric of spatial variability, its integration into a quantitative mapping framework linked to model-referenced source contributions represents the key contribution of this study. Regional contribution (RC) derived from WRF–CAMx source tagging is used as a reference benchmark to establish and evaluate the CV-RC relationship. This positions the proposed framework as a bridge between observation-based diagnostics and model-based source apportionment. The objectives are to (1) examine whether CV captures changes in local-regional dominance under different pollution levels, (2) evaluate the temporal and spatial stability of the CV–RC relationship, and (3) assess its applicability across pollutants and cities with different emission and meteorological characteristics. The framework is evaluated using a representative case study in Linyi, with Xi'an and Beijing included for inter-city comparison. Rather than replacing full source-apportionment modeling, the

proposed framework is intended as a complementary and interpretable screening tool that uses routinely available monitoring data to assess local–regional contribution balance. In this sense, it provides a bridge between observation-based variability analysis and process-based source apportionment, enabling a more direct and scalable interpretation of urban air pollution dynamics.

2. Materials and Methods

2.1. Study Area, Monitoring Data, and Modeling Configuration

Linyi is located in eastern Shandong Province, China, and was selected as the primary study area. The city is characterized by mixed industrial and traffic emissions and represents a typical medium-sized urban system. In Linyi, a multi-tier air quality monitoring network is available, including 7 national monitoring stations, 19 provincial stations, and 145 township-level stations. These stations measure pollutants (PM_{10}, $PM_{2.5}$, NO_2 and O_3) as well as key meteorological parameters. Seven national air quality monitoring stations were included in the core analysis, as shown in Figure 1. Monitoring data for Linyi were obtained from the Linyi Air Quality Monitoring and Management Platform.

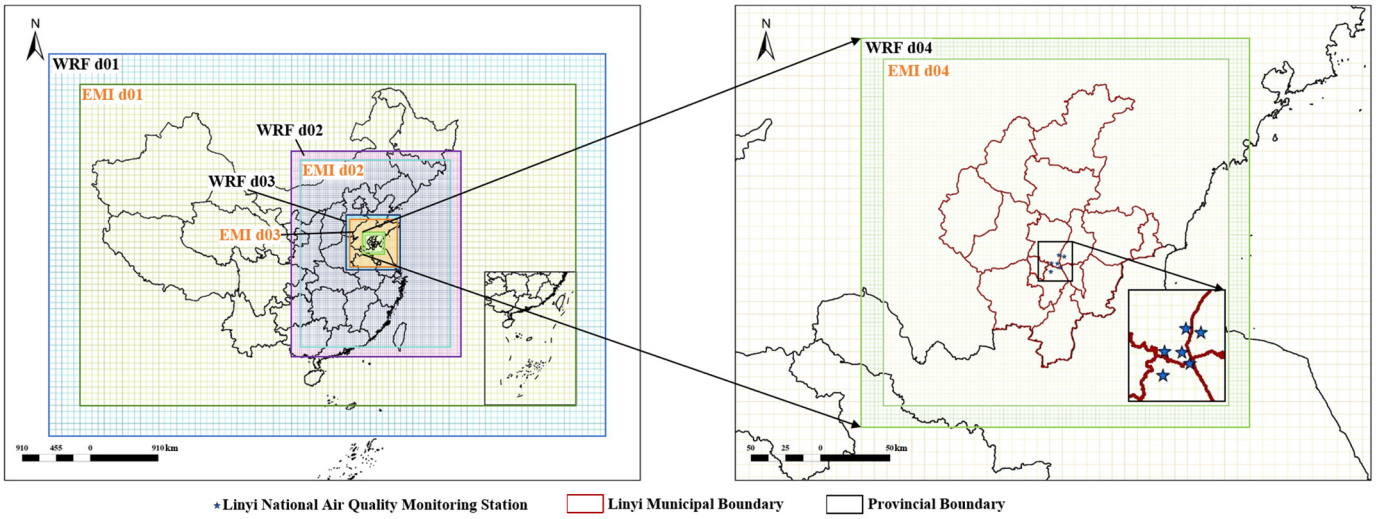

Figure 1. Nested modeling domains and grid configuration for the Linyi study area. The four domains have horizontal resolutions of 81 km, 27 km, 9 km, and 3 km, respectively. The innermost domain covers the Linyi municipal region used for local contribution analysis.

For the comparison cities, monitoring data for Xi'an were obtained from the Shaanxi Provincial Air Quality Monitoring Platform. Monitoring data for Beijing were obtained from the Beijing Municipal Ecological and Environmental Monitoring Center platform. Meteorological data were obtained from the National Meteorological Science Data Center. All datasets were derived from official monitoring networks and complied with national quality control standards.

To quantify local and regional contributions, the WRF–CAMx modeling system was applied for air quality simulation. The key parameterization schemes of the WRF–CAMx modeling system are summarized in Table 1. Four nested domains were configured with horizontal resolutions of 81 km × 81 km, 27 km × 27 km, 9 km × 9 km, and 3 km × 3 km. The Lambert conformal projection was adopted for all domains.

Within Linyi, the 2020 local emission inventory was used. For other regions in China, the 2020 Multi-resolution Emission Inventory for China was applied. For regions outside China, the 2010 MIX emission inventory was adopted. The model grid configuration is shown in Figure 1.

Table 1. Key physical and chemical parameterization schemes in the WRF–CAMx modeling system.

Model	Parameter	Configuration
WRF	Projection	Lambert conformal
	Nesting option	Three-way feedback
	Boundary conditions	NCEP reanalysis data (1° × 1°)
	Microphysics scheme	WSM 6-class
	Shortwave radiation	Goddard
	Longwave radiation	RRTM
	Planetary boundary layer	YSU
	Land surface model	Noah
	Cumulus parameterization	Kain–Fritsch
CAMx	Horizontal advection	PPM
	Gas-phase chemistry	CB05
	Aerosol chemistry	CF
	Photolysis rates	TOMS ozone dataset
	Plume-in-grid module	Off

The selection of the 2020 emission inventory is primarily constrained by data availability and consistency. This dataset represents an officially compiled and quality-controlled emission inventory that is consistent with the modeling configuration and regional emission characterization adopted in this study. It should be noted that the emission inventory year (2020) is not fully consistent with the observational dataset (2022). However, the WRF–CAMx simulation in this study is not intended to reproduce absolute pollutant concentrations for a specific year. Instead, it is used to provide a physically consistent reference for the relative contribution ratio (RC) between local and regional sources. The subsequent analysis focuses on the statistical relationship between concentration variability (CV) derived from observations and RC derived from model simulations, rather than direct time-matched concentration comparisons. Therefore, the influence of this temporal mismatch on the CV–RC relationship is expected to be limited. In addition, the CV–RC mapping is based on normalized indicators and structural relationships, which are generally less sensitive to interannual variations in emission magnitude and more dependent on the spatial distribution of emissions and atmospheric transport processes. Over short time scales, the spatial emission structure is typically more stable than absolute emission levels.

For source-tagging configuration, the Yi River Community station was defined as the spatial center. National control stations located within a 10 km radius of this station were treated as the local area, and emissions within this range were defined as local sources. This radius was selected to maintain consistency with the spatial scale used for the calculation of inter-station CV, so that the observation-derived variability metric and the model-derived local–regional RC refer to the same urban-scale domain. In addition, a 10 km radius represents a typical urban-core scale for the central Linyi area, which is sufficiently large to include multiple national monitoring stations while still focusing on predominantly local emission influences. Emissions from surrounding cities within and outside Shandong Province were treated as regional sources.

Model performance was evaluated by comparing simulated concentrations of PM_{10}, $PM_{2.5}$, O_3, and NO_2 in Linyi for the year 2022 with observations from the national monitoring network. Although the emission inventory corresponds to 2020, the evaluation focuses on the model's ability to reproduce temporal variability and spatial patterns rather than exact concentration levels. Four statistical metrics were calculated, including the correlation coefficient (R), mean bias (MB), normalized mean bias (NMB), and normalized mean error (NME). The detailed evaluation results are summarized in Table 2. According to commonly used evaluation criteria for air quality models (e.g., U.S. EPA guidelines),

acceptable performance is typically characterized by $|NMB| \leq 30\%$ and $NME \leq 50\%$ for particulate matter, although criteria may vary by pollutant and application.

Table 2. Performance statistics of WRF–CAMx simulations in Linyi in 2022.

Pollutant	R	MB (μg/m^3)	NMB (%)	NME (%)
PM_{10}	0.63	−52.36	−42.19	46.29
$PM_{2.5}$	0.58	−28.54	−30.86	39.21
O_3	0.500	−33.58	−77.02	77.02
NO_2	0.69	14.11	33.57	39.76

Overall, the model reproduces the temporal variability of pollutant concentrations with correlation coefficients ranging from 0.50 to 0.69, while bias metrics show pollutant-dependent differences. Although discrepancies exist in absolute concentration levels, such performance is comparable to commonly reported ranges in regional air quality modeling studies.

In this study, the WRF–CAMx simulation is not used to reproduce exact concentrations, but to provide a physically consistent reference for the relative local–regional contribution ratio (RC). Since RC is a relative metric, it is less sensitive to systematic bias in concentration magnitude. Therefore, the model performance is considered sufficient to support the CV–RC analysis.

2.2. Quantification of Concentration Variability Among Monitoring Stations

Concentration variability among monitoring stations was quantified using the coefficient of variation. At each time step t, the spatial mean concentration across all stations is defined as:

$$\mu_t = \frac{1}{N}\sum_{i=1}^{N} C_{i,t}$$

The spatial standard deviation is:

$$\sigma_t = \sqrt{\frac{1}{N}\sum_{i=1}^{N}\left(C_{i,t} - \mu_t\right)^2}$$

The coefficient of variation at time t is therefore:

$$CV_t = \frac{\sigma_t}{\mu_t}$$

where $C_{i,t}$ denotes the concentration at station i and time t, N is the number of monitoring stations, μ_t is the spatial mean concentration, σ_t is the spatial standard deviation, CV_t is the concentration variability among monitoring stations index. In addition to the CV, which quantifies spatial variability among monitoring stations at a given time, a secondary metric, denoted as CV_v, is introduced to characterize the temporal variability of CV. For a given spatial scale (i.e., a defined station subset), a time series of CV values is first calculated. The metric CV_v is then obtained by applying the coefficient of variation formula to this CV time series. Therefore, CV_v represents the temporal dispersion of inter-station variability, describing how stable or fluctuating the spatial heterogeneity is over time. While CV reflects the instantaneous spatial contrast of pollutant concentrations, CV_v captures the temporal dynamics of that contrast. A low CV_v indicates that the spatial variability pattern is relatively stable over time, suggesting persistent emission–transport conditions, whereas a high CV_v reflects strong temporal fluctuations in spatial heterogeneity, which may be associated with rapidly changing meteorological conditions or emission patterns. This

metric provides additional information beyond CV by distinguishing between steady and transient variability regimes, and is therefore useful for interpreting the stability of the relationship between concentration variability and regional contribution. Together, CV and CV_v provide a complementary description of spatial heterogeneity and its temporal stability in urban air pollution.

To construct the mapping between variability and regional contribution, concentration segmentation was performed based on the time series of spatial mean concentration μ_t. The mean concentration values were divided into equal-interval bins. Interval widths were selected to ensure sufficient sample size within each bin and to cover the full concentration range of each pollutant. Let the concentration range be bounded by the minimum and maximum values in the dataset. The number of intervals, denoted as I, depends on the selected interval width and the data range. For each time step t, the corresponding spatial mean concentration μ_t was assigned to one of these intervals. Different pollutants adopted different interval widths to ensure adequate representation of their concentration distributions, and the detailed binning scheme is provided in Table S1 in the Supplementary Materials.

The selection of bin widths was guided by the need to balance statistical robustness and resolution of concentration variability. Therefore, relatively fine and uniformly spaced intervals were adopted to avoid overly coarse aggregation. Given the relatively small interval widths and the continuous stratification across the full concentration range, the binning scheme is expected to have a limited influence on the fitted relationships.

2.3. Calculation of Regional Contribution Ratio

Regional contribution ratios were derived from WRF–CAMx source-tagging simulations. At each time step t, total simulated concentration $C_{total,t}$ and locally tagged concentration $C_{local,t}$ were extracted. The regional contribution ratio is defined as:

$$RC_t = 1 - \frac{C_{local,t}}{C_{total,t}}$$

where RC_t is the regional contribution ratio at time t, $C_{local,t}$ is the modeled concentration from local emissions, $C_{total,t}$ is the modeled total concentration.

2.4. Construction of the CV–RC Mapping Framework

The analytical framework links monitoring-derived variability with model-derived regional contributions through a concentration-segmentation approach.

First, time-series mean concentrations μ_t were divided into equal-interval concentration bins according to pollutant-specific ranges. The number of intervals depends on the minimum and maximum values of the dataset.

For each concentration interval k, corresponding arrays of CV_t and RC_t were grouped. The mean variability and mean regional contribution within interval k were computed as:

$$\overline{CV}_k = \frac{1}{n_k}\sum_{j=1}^{n_k} CV_{k,j}$$

$$\overline{RC}_k = \frac{1}{n_k}\sum_{j=1}^{n_k} RC_{k,j}$$

where n_k is the number of samples in interval k, $CV_{k,j}$ and $RC_{k,j}$ are the values within that interval.

A regression function was then fitted using $\overline{CV}_k$ as the independent variable and $\overline{RC}_k$ as the dependent variable:

$$\overline{RC}_k = f(\overline{CV}_k)$$

The CV–RC mapping was constructed using the full-year dataset (2022) to ensure that the fitted relationship captures a wide range of concentration conditions and variability regimes. For each pollutant, all available hourly observations within the study year were used to derive the concentration-segmented CV–RC relationship.

To evaluate the applicability of the derived mapping under realistic pollution conditions, a temporally independent subset of the data (January 2022) was used for application-based assessment. Although both datasets originate from the same year, this temporal separation provides a quasi-independent evaluation of the mapping performance under different pollution regimes.

Regression forms included power-law, exponential, and linear functions. Model performance was evaluated using the coefficient of determination R^2 and statistical significance test. Among these, the power-law function generally provided the most consistent fit across different pollutants and scales.

Finally, the fitted function was applied to monitoring-derived CV_t to estimate real-time regional contribution ratios:

$$RC_t^{est} = f(CV_t)$$

Based on the derived estimation model, local and regional contributions can be rapidly estimated using monitoring data only. The temporal resolution of the estimated contribution ratio is consistent with the temporal resolution of the input monitoring data. The concentration variability among monitoring stations at time t, denoted as CV_t, is calculated from monitoring observations. The calculated CV_t is substituted into the fitted regression function to obtain the estimated regional contribution ratio RC_t^{est}. The local contribution ratio at time t is then calculated as:

$$LC_t = 1 - RC_t$$

where RC_t denotes the regional contribution ratio at time t derived from the estimation model, LC_t denotes the local contribution ratio at time t. This formulation ensures that the total contribution is conserved at each time step.

2.5. Temporal and Spatial Scale Configuration

To evaluate the applicability and robustness of the proposed rapid estimation method for local contributions based on concentration variability among monitoring stations, we examined its performance at different temporal and spatial scales.

Hourly concentration data were used as the base dataset. Daily mean concentrations were calculated as the arithmetic mean of valid hourly values within each day. Monthly mean concentrations were calculated from daily averages. Inter-station variability and regional contribution ratios were calculated separately at each temporal scale. Separate regression models between CV and RC were developed for hourly, daily, and monthly data. This analysis was used to examine the stability of the relationship at different temporal scales.

For spatial assessment in Linyi, the Yi River Community national station is selected as the urban center. Circular buffers with radii of 10, 15, 20, 25, 30, and 40 km are defined. As illustrated in Figure 2, these spatial scales are constructed as nested buffers, within which monitoring stations are progressively included to form nested station subsets with increasing sample size. For each spatial scale, the CV is calculated at each time step using all stations within the corresponding subset, resulting in a time series of CV values specific to that spatial scale. The temporal variability of CV, denoted as CV_v, is then computed

by applying the coefficient of variation formula to this CV time series. Therefore, CV_v is calculated independently for each spatial scale and represents the temporal variability of spatial heterogeneity within that scale. Inter-station variability and the corresponding CV-RC regression models were recalculated for each spatial range. This analysis was used to assess the influence of spatial extent and station number on estimation stability.

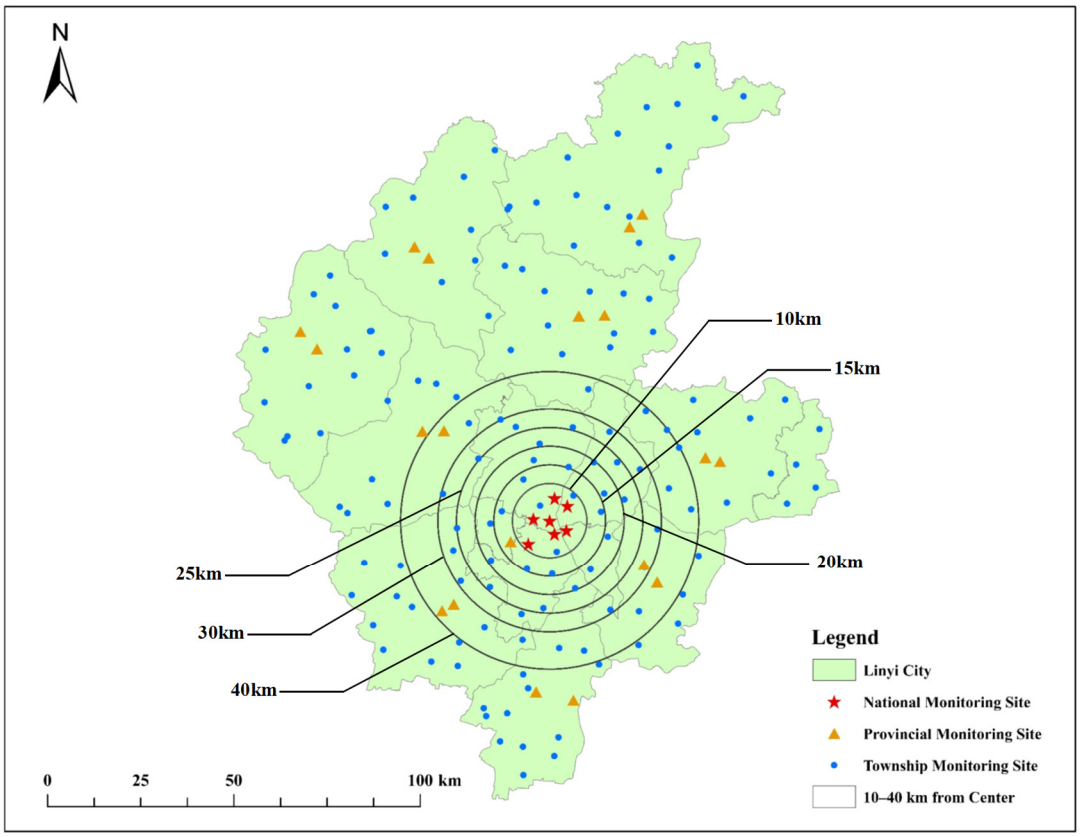

Figure 2. Spatial distribution of monitoring stations and nested buffer zones (10–40 km) used for multi-scale analysis of CV and CV_v in Linyi.

For cross-city analysis, the same spatial configuration was applied in all cities to ensure comparability. In Xi'an and Beijing, the monitoring stations located at the urban centers were selected as reference points. A 10 km buffer was defined in each city. National monitoring stations located within this range were included. The same 10 km buffer was also applied in Linyi for comparison.

Estimation performance was evaluated by comparing the estimated regional contribution ratios (RC_{est}), derived from the CV-based framework, with the model-derived regional contribution ratios (RC_{mod}) obtained directly from the WRF–CAMx simulations. It should be emphasized that this evaluation is conducted on regional contribution ratios, and is intended to assess the consistency between the observation-based estimation approach and the model-based source apportionment. All available time steps with valid paired RC_{est} and RC_{mod} values were included in the evaluation, without random subsampling. The number of samples is therefore determined by data completeness after quality control. Evaluation metrics included the Pearson correlation coefficient and the coefficient of determination. Statistical significance was tested at a 95% confidence level. Performance across pollutants, temporal scales, and spatial ranges was compared to assess robustness.

Four statistical metrics were adopted: the correlation coefficient (R), mean bias (MB), normalized mean bias (NMB), and normalized mean error (NME). In this study, the R is used to evaluate the strength of agreement between estimated and modeled values,

while the coefficient of determination (R^2) is used in regression analyses to quantify the goodness-of-fit and explanatory power of the CV–RC relationship. The calculation formulas are:

$$MB = \overline{RC_{est}} - \overline{RC_{mod}}$$

$$R = \sqrt{\frac{\left[\sum_{i=1}^{N}\left(RC_{est,i} - \overline{RC_{est}}\right)\left(RC_{mod,i} - \overline{RC_{mod}}\right)\right]^2}{\sum_{i=1}^{N}\left(RC_{est,i} - \overline{RC_{est}}\right)^2 \sum_{i=1}^{N}\left(RC_{mod,i} - \overline{RC_{mod}}\right)^2}}$$

$$NMB = \frac{\sum_{i=1}^{N}(RC_{mod,i} - RC_{est,i})}{\sum_{i=1}^{N} RC_{est,i}}$$

$$NME = \frac{\sum_{i=1}^{N}|RC_{est,i} - RC_{est,i}|}{\sum_{i=1}^{N} RC_{est,i}}$$

where RC_{est} and RC_{mod} represent the mean estimated and model-derived regional contribution ratios, respectively; $RC_{est,i}$ and $RC_{mod,i}$ denote the estimated and modeled regional contribution ratios at time step i, respectively, and N is the total number of samples.

This nested-buffer design ensures that spatial-scale effects are evaluated using consistent, progressively expanding station subsets rather than independent regional partitions. Specifically, the analysis employs a nested-subset approach in which a corresponding station subset is identified for each spatial scale, the CV is computed at each time step, and CV_v is subsequently derived from the resulting CV time series.

3. Results and Discussion

3.1. Spatiotemporal Characteristics of Concentration Variability Among Monitoring Stations

Concentration variability among monitoring stations is affected by spatial extent, local emissions, meteorological dispersion, and regional transport. Understanding its temporal patterns and spatial-scale sensitivity is the basis for linking inter-station differences with local and regional contributions. To ensure the robustness of the analysis, multi-year observations from 2019 to 2022 were first examined to evaluate the temporal stability of inter-station CV patterns (Figures 3 and 4). The results indicate consistent seasonal and diurnal structures across years, with only minor interannual differences. Based on this demonstrated stability, the year 2022 was selected as a representative case for detailed analysis in the subsequent sections, due to its relatively comprehensive data availability after quality control and its consistency with the WRF–CAMx simulation period used to derive RC.

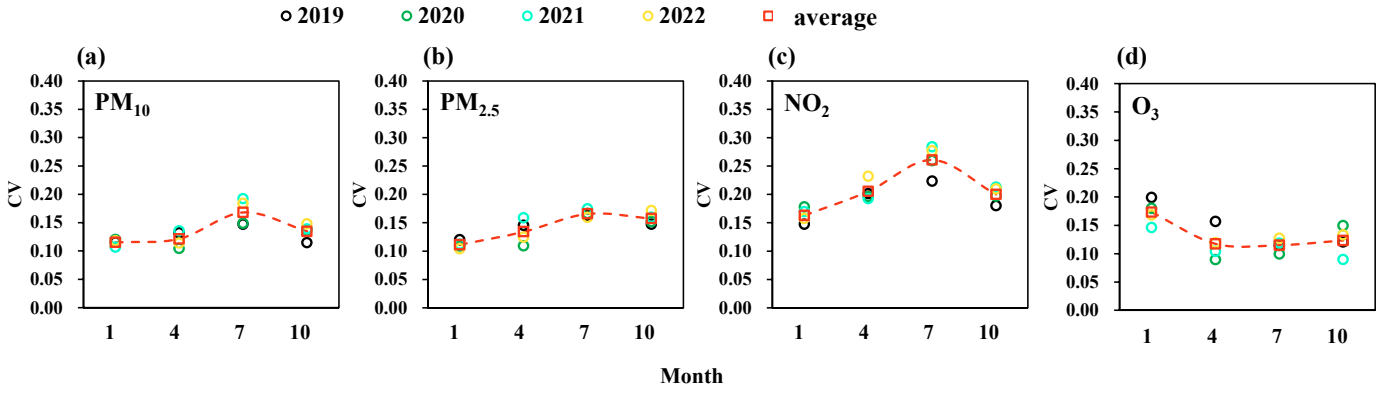

Figure 3. Seasonal variation in concentration CV among monitoring stations within the 25 km urban domain of central Linyi during four representative months (January, April, July, and October), corresponding to the four seasons from 2019 to 2022: (**a**) PM_{10}, (**b**) $PM_{2.5}$, (**c**) NO_2, (**d**) O_3.

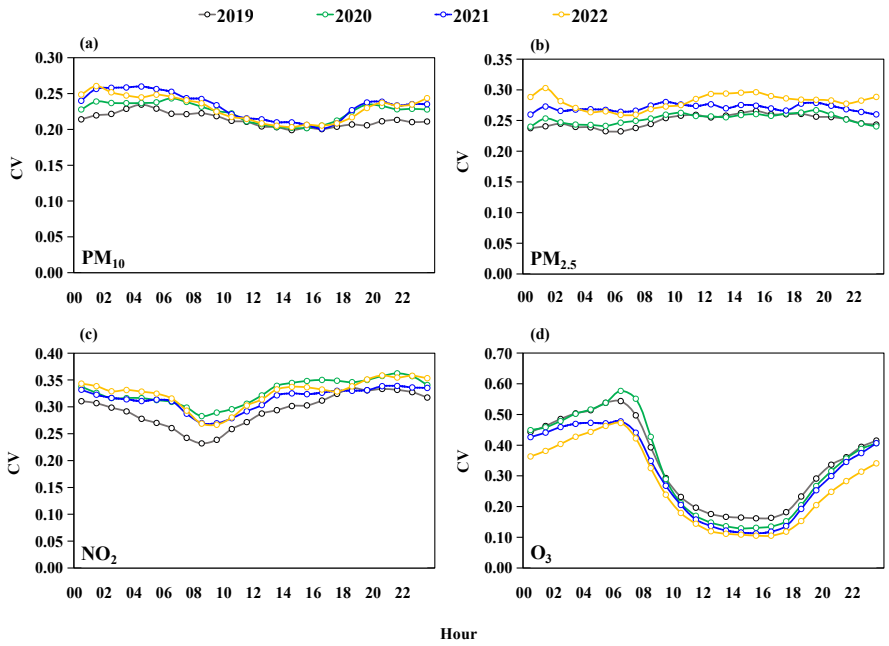

Figure 4. Diurnal variation in concentration CV among monitoring stations within the 25 km urban domain of central Linyi during 2019–2022: (**a**) PM_{10}, (**b**) $PM_{2.5}$, (**c**) NO_2, (**d**) O_3.

This section analyzes four pollutants (PM_{10}, $PM_{2.5}$, O_3, and NO_2) from three aspects: (1) temporal characteristics under a fixed spatial range at different time resolutions; (2) spatial characteristics under different station coverage radii; and (3) inter-city comparison under a unified 10 km configuration.

3.1.1. Temporal Characteristics: Typical Months and Diurnal Variation

To characterize the temporal structure of concentration variability among monitoring stations, a full monthly analysis (January–December) was first conducted for multiple years (2018–2022). Based on the consistent seasonal patterns observed across the full dataset, four representative months (January, April, July, and October), corresponding to winter, spring, summer, and autumn, were selected within the 25 km urban domain of central Linyi (Figure 3). These representative months are used solely for descriptive analysis of seasonal patterns and visualization purposes, and do not constitute an independent dataset for model development or validation. The full monthly results are provided in the Supplementary Materials (Figure S1). The corresponding seasonal mean concentrations for these representative months are summarized in Table S1. Diurnal patterns were further examined using hourly data (Figure 4), and the corresponding diurnal mean concentrations are provided in Table S2. These representative months were selected to capture the characteristic seasonal conditions (winter, spring, summer, and autumn) and to provide a clear and concise illustration of the seasonal variability. This contrast reflects differences in the relative influence of local emissions and regional transport among pollutants.

Overall, seasonal patterns were consistent across the four years, and interannual differences were small. The full monthly analysis further confirms that these seasonal structures are stable across all months, with consistent peak and low-CV periods. This indicates that the inter-station CV exhibits a relatively stable seasonal structure, shown as Figure 3. PM_{10}, $PM_{2.5}$, and NO_2 showed similar seasonal behavior. CV increased from winter to summer, reached higher values in July, and then decreased. PM_{10} presented relatively low CV in January and April. $PM_{2.5}$ showed lower CV in winter. These patterns suggest that regional transport and enhanced large-scale mixing tend to reduce spatial differences during these periods. In contrast, NO_2 exhibited a larger seasonal amplitude, indicating

stronger sensitivity to local emission contrasts. O_3 displayed a different pattern. During April, July, and October, when O_3 pollution was more pronounced, CV remained relatively low. This indicates that under conditions dominated by regional transport and photochemical production, the urban-scale concentration field becomes more spatially uniform. In January, background O_3 levels were lower, and CV was relatively higher, suggesting stronger influence from local precursor emissions and meteorological differences.

In general, primary pollutants tended to show enhanced spatial heterogeneity in summer, whereas O_3 exhibited stronger regional coherence during its high-concentration seasons.

Hourly CV patterns showed broadly consistent diurnal structures during 2019–2022 (Figure 4). To facilitate interpretation, the corresponding diurnal mean concentrations of PM_{10}, $PM_{2.5}$, NO_2, and O_3 within the 25 km urban domain are provided in Table S2. It should be noted that, by definition, CV depends on both spatial standard deviation and mean concentration ($CV = \sigma/\mu$). Therefore, part of the diurnal variation in CV may reflect changes in mean concentration rather than changes in spatial heterogeneity alone.

For PM_{10}, CV was generally higher during the late night and early morning and lower during midday, suggesting a combined influence of concentration level and spatial heterogeneity. $PM_{2.5}$ exhibited relatively weak diurnal variability in CV, indicating that its inter-station differences remained comparatively stable throughout the day.

NO_2 showed a clear decrease in CV from nighttime to the morning period, followed by a gradual increase during the daytime. This pattern is consistent with the combined influence of changing mean concentration and evolving spatial distribution associated with traffic emissions and boundary-layer development. However, because CV is inversely related to mean concentration, this pattern should not be interpreted as a direct indicator of physical mixing alone.

For O_3, the daytime decline in CV coincided with a rapid increase in mean concentration. This indicates that a substantial portion of the CV decrease can be attributed to the mathematical dependence of CV on concentration level. Additional influences from photochemical production and regional mixing may also contribute to reduced spatial contrasts, but such mechanisms cannot be inferred from the raw diurnal CV profile alone.

Overall, the diurnal CV patterns provide a descriptive view of temporal changes in inter-station variability. A more robust interpretation of the relationship between concentration variability and regional contribution is therefore developed in Section 3.2 through concentration-stratified analysis, which reduces the direct influence of mean concentration on CV. Therefore, Figure 4 is primarily intended to provide a qualitative overview of temporal patterns in inter-station variability, rather than to support direct mechanistic inference, particularly when interpreted in a relative sense rather than as large absolute differences.

3.1.2. Spatial Characteristics: Variation in Concentration Variability Among Monitoring Stations Under Different Buffer Radii

Based on the interannual stability identified above, 2022 was selected as a representative year for detailed spatial analysis. Using 2022 data for urban Linyi, the spatial distribution of monitoring stations and the nested-buffer design are shown in Figure 2, which illustrates the relative positions of stations with respect to the defined spatial domains. Concentration variability among monitoring stations within each spatial range was compared (Figure 5).

Overall, temporal trends were consistent across different spatial ranges. However, the magnitude of CV varied significantly with buffer size. The most distinct feature is that CV within the 10 km range was clearly lower than that at larger scales. When the spatial range expanded from 10 km to 15 km, CV increased noticeably for all pollutants. Beyond 15 km, differences among larger spatial ranges became relatively small. This pattern

suggests that within the 10 km range, inter-station variability is more strongly associated with local emission contrasts, as the stations are located within a relatively compact urban core (Figure 2). When the domain expands to ≥15 km, regional transport and larger-scale mixing become more important, and the spatial structure of concentrations tends to stabilize across sites. At larger spatial scales (≥15 km), the differences among buffer sizes become less pronounced, suggesting that the inclusion of additional stations beyond this range does not substantially alter the overall spatial variability structure. This behavior is consistent with the increasing influence of regional-scale processes, including transport and mixing, which tend to reduce relative contrasts among sites. Among pollutants, the CV of NO_2 showed the strongest sensitivity to spatial scale. The CVs of PM_{10} and $PM_{2.5}$ exhibited intermediate responses, whereas the CV of O_3 showed the smallest variation across scales, reflecting its stronger regional mixing characteristics.

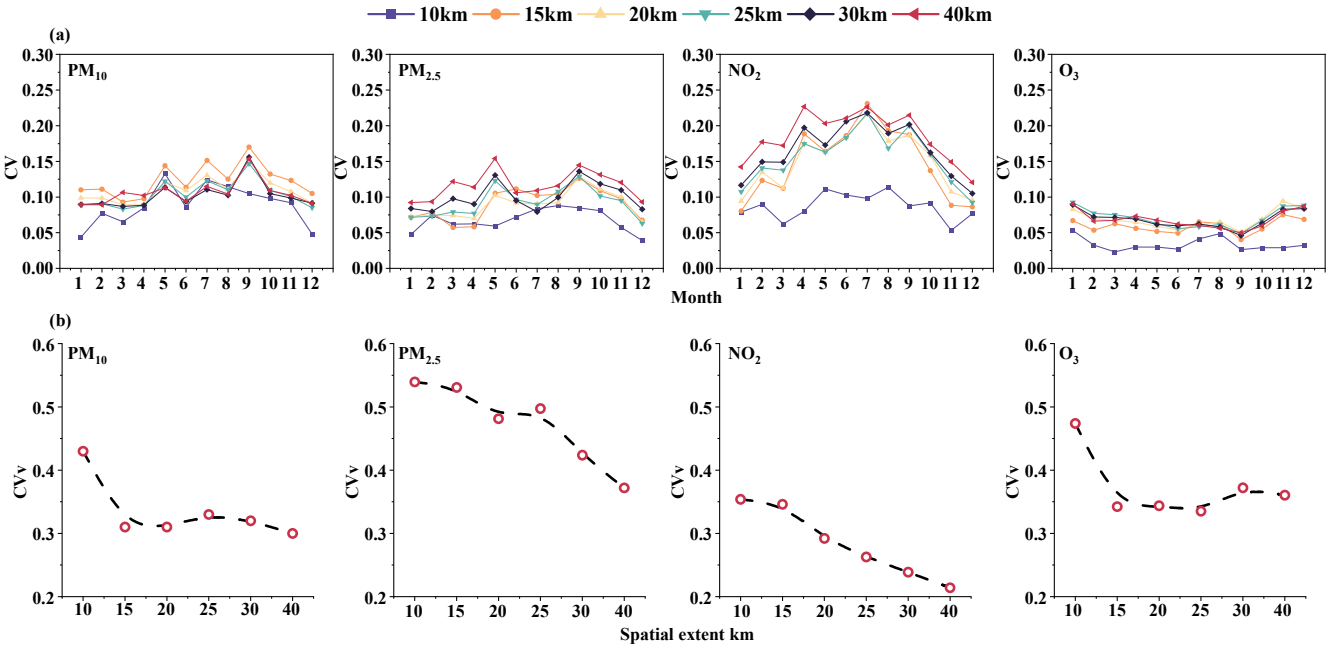

Figure 5. Comparison of concentration CV among monitoring stations for PM_{10}, $PM_{2.5}$, NO_2 and O_3 within six spatial buffers (10, 15, 20, 25, 30, and 40 km) centered on urban Linyi in 2022: (**a**) monthly variation in CV across spatial ranges from January to December 2022; (**b**) daily variation in CV across spatial ranges in 2022. The dashed lines are used to highlight the overall variation trend across different spatial scales.

The normalized variability index (CV_v) decreased as spatial range increased. This suggests that although the absolute CV level increased with larger spatial domains, the relative fluctuation amplitude was gradually smoothed by regional mixing processes.

Overall, the spatial-scale analysis further confirms that inter-station variability is jointly regulated by spatial heterogeneity of emissions and regional transport mixing. At the same time, the results are also affected by the spatial distribution and number of monitoring stations, as illustrated in Figure 2. The choice of spatial domain therefore directly affects the stability of the subsequent CV–RC mapping relationship.

3.1.3. Inter-City Comparison of Concentration Variability Among Monitoring Stations

Beijing and Xi'an were selected as representative cities for comparison with Linyi. For each city, national monitoring stations within a 10 km radius from the city center were included. Hourly CV distributions and daily CV_v in 2022 were analyzed (Figures 6 and 7).

Compared with CV, which reflects spatial heterogeneity at a given time, CV_v provides insight into the temporal stability of spatial variability patterns.

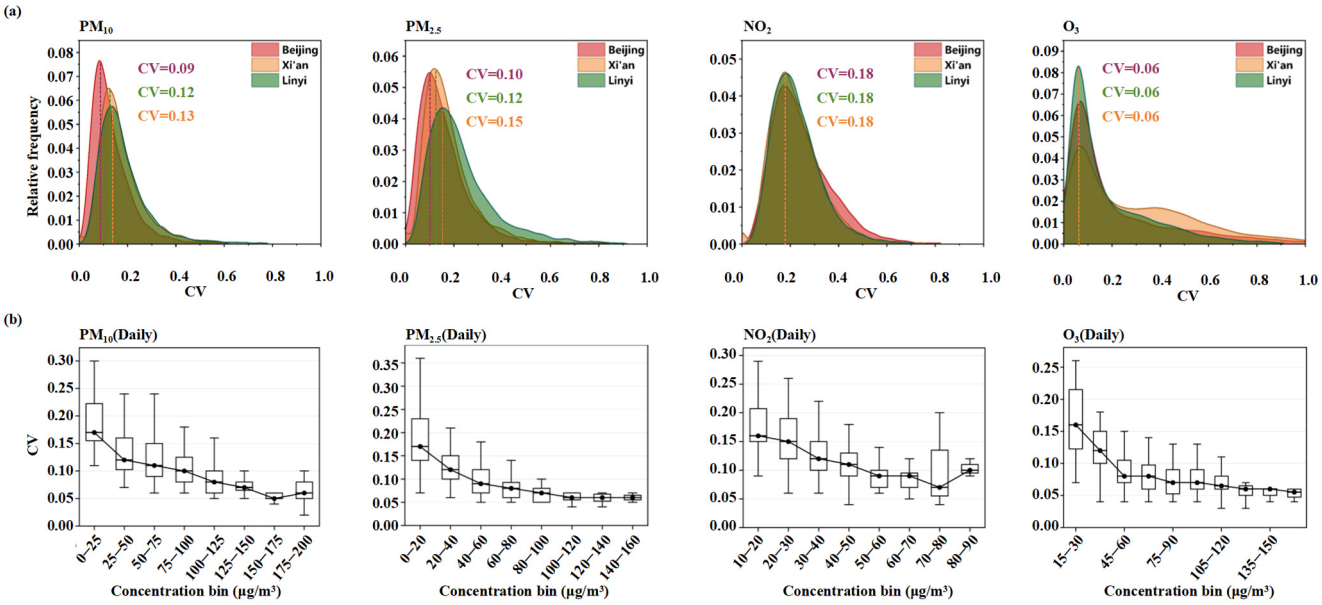

Figure 6. Integrated representation of inter-station concentration variability: (**a**) inter-city comparison of hourly CV distributions within the 10 km urban domains in 2022 for PM_{10}, $PM_{2.5}$, NO_2, and O_3 in Linyi, Xi'an, and Beijing; (**b**) concentration-stratified distributions of CV at the daily scale in Linyi for PM_{10}, $PM_{2.5}$, NO_2, and O_3.

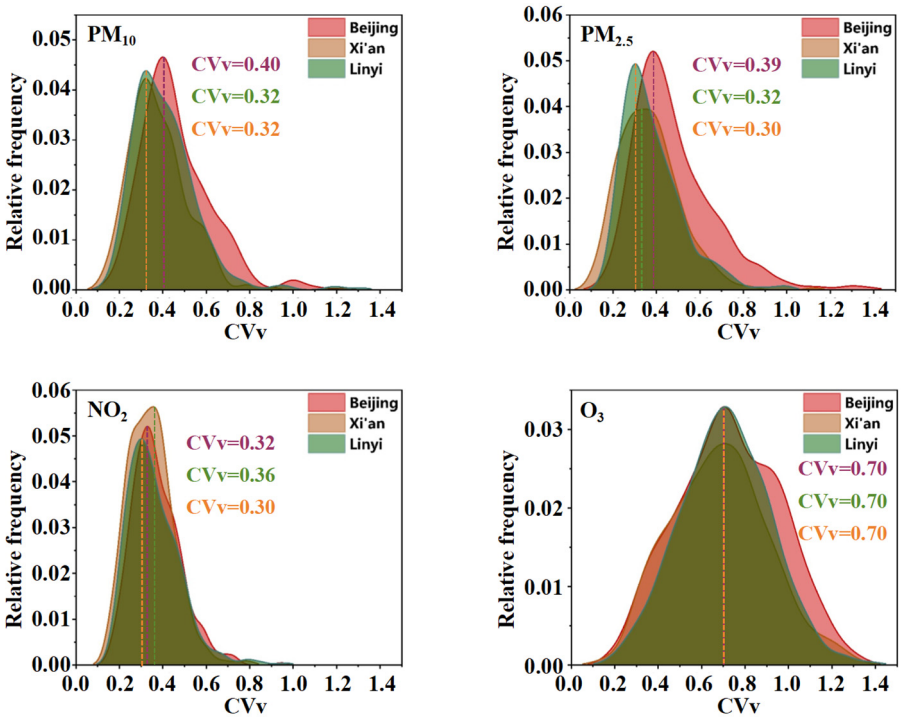

Figure 7. Inter-city comparison of inter-station variability within the 10 km urban domain in 2022: probability distributions of daily variability of hourly CV (CV_v) in Linyi, Xi'an, and Beijing.

As shown in Figure 6a, for PM_{10} and $PM_{2.5}$, the peak values of hourly CV followed the order: Linyi > Xi'an > Beijing. Within the same 10 km spatial domain, these differences suggest that Linyi exhibits stronger inter-station concentration contrasts. This may be associated with differences in emission distribution, urban structure, and meteorological

conditions. Compared with Xi'an, terrain constraints and relatively low wind speeds in Xi'an favor pollutant accumulation and mixing within the urban area, which may reduce spatial contrasts among stations. In Beijing, relatively improved air quality and a more uniform emission structure contribute to a stronger influence of regional transport during pollution episodes, resulting in lower CV values within the same spatial domain. For NO_2 and O_3, differences in peak hourly CV among the three cities were relatively small. The CV of O_3, influenced by regional transport and photochemical processes, showed limited inter-city differences at the urban scale. NO_2 exhibited relatively high CV values in all three cities, reflecting strong intra-urban emission contrasts, although differences among cities were not pronounced. Figure 6b, which will be discussed in Section 3.2.1, presents the concentration-stratified behavior of CV at the daily scale.

Overall, particulate matter displayed clearer inter-city differences in hourly CV, whereas the CV of O_3 showed the smallest differences, and the CV of NO_2 exhibited consistently high variability across cities.

Daily variability of hourly CV was further evaluated using CV_v (Figure 7). For PM_{10} and $PM_{2.5}$, the peak CV_v values followed the order: Beijing > Xi'an ≈ Linyi. This suggests stronger intra-day fluctuations of concentration variability in Beijing. In contrast, Xi'an and Linyi exhibited relatively more stable CV_v patterns.

NO_2 showed similar peak CV_v values across the three cities. Although NO_2 is mainly associated with mobile sources, its intra-day variability was comparable among cities. O_3 presented nearly unchanged CV_v distributions across the three cities, and its daily fluctuation amplitude remained lower than that of NO_2.

These inter-city results indicate that both the magnitude and temporal fluctuation of inter-station variability differ among pollutants and urban environments. However, the interpretation is constrained by differences in station distribution and local urban characteristics, which should be considered when comparing variability across cities.

Taken together, the analyses in Section 3.1 demonstrate that inter-station variability exhibits systematic temporal regularity, spatial-scale dependence, and inter-city differentiation. These structural characteristics indicate that CV is not random fluctuation but reflects organized emission–transport interactions, providing the empirical foundation for constructing a quantitative linkage with regional contribution ratios.

In a broader context, these spatiotemporal patterns are consistent with previous studies showing that intra-urban variability of air pollutants is governed by the interplay between emission heterogeneity and atmospheric transport processes [42,46]. For primary pollutants, enhanced variability reflects uneven emission distributions under limited dispersion conditions, whereas reduced variability during high-concentration periods, particularly for O_3, indicates the increasing influence of regional transport and photochemical production, which tend to homogenize urban concentration fields [38]. These results suggest that inter-station CV captures organized emission–transport dynamics rather than random fluctuations, providing a physical basis for subsequent quantitative linkage with regional contribution ratios.

3.2. Drivers and Physical Interpretation of CV Variation

3.2.1. CV Variation Under Different Pollution Levels

Figure 6b presents the concentration-stratified distributions of the CV for $PM_{2.5}$, PM_{10}, NO_2, and O_3 at both daily scale, while the corresponding hourly scale results are provided in Figure S4. By grouping data into concentration bins and summarizing CV using boxplots, this approach reduces the direct functional coupling between CV and concentration ($CV = \sigma/\mu$), allowing CV variability to be interpreted beyond a purely mathematical constraint. In addition to the median CV, the spread of CV within each concentration

bin (represented by interquartile range and boxplot distribution) is used as an estimate of variability and uncertainty, allowing the statistical significance of differences across concentration levels to be assessed.

Across all pollutants, median CV generally decreases with increasing concentration. However, the variability of CV within each bin does not decrease uniformly across pollutants or temporal scales. The spread of CV values, as reflected by the interquartile range, provides an estimate of uncertainty and demonstrates that the observed differences across concentration levels are statistically meaningful rather than arising from random fluctuation.

For $PM_{2.5}$ and PM_{10}, both median CV and interquartile range (IQR) decrease systematically with increasing concentration at the daily scale. For $PM_{2.5}$, the median CV decreases from approximately 0.17–0.18 to 0.05–0.06 (about 65–70%), while the IQR decreases by roughly 40–50%. This suggests that high-pollution conditions correspond to more spatially homogeneous concentration fields. At the hourly scale, similar trends are observed, although variability remains larger due to short-term fluctuations in emissions and meteorology (Figure S2). Compared with gaseous pollutants, particulate matter exhibits intermediate behavior. $PM_{2.5}$ is more strongly influenced by secondary formation and regional transport processes, whereas PM_{10} retains a larger contribution from primary emissions, resulting in a mixed response in spatial variability.

In contrast, NO_2 exhibits a clear scale dependence. At the hourly scale, the median CV decreases from approximately 0.30 to 0.15, whereas at the daily scale it remains within a narrower range (about 0.15–0.10), showing a much weaker dependence on concentration. This reflects the strong influence of diurnal emission patterns (e.g., traffic), as well as the short atmospheric lifetime of NO_2 (on the order of hours), which limits its spatial dispersion and leads to strong sensitivity to local emission contrasts. As a result, NO_2 exhibits pronounced spatial heterogeneity, particularly at shorter temporal scales.

For O_3, CV decreases with concentration at both temporal scales, but the reduction in variability is weaker than for particulate matter. This behavior can be explained by its nature as a secondary pollutant with a relatively long effective atmospheric lifetime and strong regional photochemical production, which tends to produce spatially coherent concentration fields. However, near-surface titration by NO emissions, particularly at night, may introduce localized variability under certain conditions.

To interpret the physical implications, the co-variation in CV magnitude and variability across concentration bins provides key insight. While the decrease in CV is partly expected from its definition, the concurrent reduction (or persistence) of variability indicates that low CV values are associated with spatially coherent fields dominated by regional transport, whereas high and unstable CV values reflect stronger local emission influence.

Overall, these results demonstrate that CV captures not only the magnitude of spatial heterogeneity but also its stability across concentration regimes. Similar concentration-dependent reductions in spatial variability have been reported in previous studies, where regional accumulation and synoptic-scale transport lead to more spatially homogeneous pollution fields [27,38]. In contrast, locally dominated conditions, especially under low concentrations or weak mixing, tend to amplify inter-site differences due to heterogeneous emission sources [42,46]. Compared with these studies, the present analysis further shows that both the magnitude and variability of CV evolve systematically with concentration, providing a more robust statistical indicator that reflects not only spatial contrasts but also their stability. This dual sensitivity strengthens the interpretation of CV as a dynamic proxy for emission–transport balance, directly supporting its use in constructing a quantitative CV–RC relationship.

3.2.2. Dependence of Inter-Station Coefficient of Variation on Wind Direction and Wind Speed

To further examine the meteorological drivers of inter-station variability, the influence of wind direction and wind speed was analyzed for the three cities in 2022. The corresponding results are provided in the Supplementary Materials (Figures S3 and S4).

The influence of wind direction on inter-station CV is shown in Figure S3a. Among all pollutants, the CV of O_3 showed the strongest wind direction dependence. In Beijing, CV values ranged from 0.14 to 0.32. In Xi'an, values ranged from 0.27 to 0.44. In Linyi, the CV of O_3 varied between 0.13 and 0.30. These large directional contrasts, together with the dominant wind patterns (Figure S3b), indicate strong sensitivity to transport-related processes. For PM_{10} and $PM_{2.5}$, directional differences in CV were moderate. In Beijing, minimum CV values occurred under southerly or southeasterly winds (0.11 for PM_{10} and 0.14 for $PM_{2.5}$), while maximum values appeared under northerly sectors (0.15 and 0.20, respectively). In Xi'an, variations were small (0.02–0.04). In Linyi, the CV of $PM_{2.5}$ ranged from 0.20 to 0.26 depending on wind sector. The CV of NO_2 showed relatively high CV levels in all three cities, but directional contrasts were weaker than those of O_3. In Beijing, CV ranged from 0.20 to 0.31. In Linyi, values ranged from 0.20 to 0.26. Sectoral variation in Xi'an was limited.

In addition to wind direction, the influence of wind speed was further examined using windspeed stratified boxplots of the CV for each pollutant ($PM_{2.5}$, PM_{10}, NO_2, and O_3) (Figure S4), in order to directly evaluate its role in modulating inter-station variability. The results show that the response of inter-station CV to wind speed is pollutant-dependent. For primary pollutants ($PM_{2.5}$, PM_{10} and NO_2), median CV values remain relatively stable across wind-speed bins, with only modest variations and a slight tendency toward increased variability at intermediate wind speeds. In contrast, the CV of O_3 exhibits a clear decreasing trend with increasing wind speed, indicating enhanced spatial homogenization under stronger wind conditions due to increased atmospheric mixing and regional transport. For higher wind-speed bins (>7 m/s), the number of samples becomes limited for all pollutants, and the distributions exhibit larger variability.

Overall, the combined wind-direction and wind-speed analyses demonstrate that CV dynamically responds to meteorological forcing, with wind direction controlling transport pathways and wind speed modulating the balance between local accumulation and regional advection. Similar dependencies of pollutant variability on wind conditions have been reported in previous studies, where directional transport and ventilation efficiency strongly influence spatial concentration patterns [27,40]. However, the present results further indicate that the response of CV to wind speed is not monotonic, but varies among pollutants, reflecting the competing effects of dispersion, organized transport, and source heterogeneity. This highlights that increased wind speed does not necessarily lead to spatial homogenization, but may instead enhance contrasts when strong advection introduces heterogeneous upwind sources. Such behavior provides additional evidence that CV integrates multiple physical processes, reinforcing its suitability as a composite indicator of emission–transport interactions under varying meteorological conditions.

3.2.3. Local Emission Versus Regional Transport Dominance

Given the nonlinear nature of O_3 formation chemistry, the variability of O_3 reflects the combined influence of chemical processes and transport dynamics. It should be noted that the analysis presented here focuses on selected high-CV periods for O_3 and is intended to provide a process-level illustration of the relationship between local emissions and inter-station variability. These short-term episodes are not meant to represent the full temporal behavior of all pollutants.

The generality of CV responses across pollutants and over the full time series has been systematically evaluated in Section 3.2.1 (Figures 6b and S2), where consistent concentration-dependent patterns are observed for $PM_{2.5}$, PM_{10}, NO_2, and O_3 at both daily and hourly scales. In this context, the present analysis serves as a complementary case-based interpretation to elucidate the underlying mechanisms driving the statistical relationships identified at the full time-series level.

These results highlight that the spatial variability of O_3 is governed by the combined effects of photochemical production, transport, and local titration processes, reflecting its nature as a secondary pollutant with a relatively long atmospheric lifetime. Previous studies have shown that O_3 concentrations are largely controlled by regional-scale photochemical production and long-range transport, leading to relatively homogeneous concentration fields under polluted conditions [38,40]. This explains the generally low CV values observed during high-O_3 periods in Section 3.2.1. However, the elevated CV observed during selected high-variability episodes indicates that local processes can still modulate spatial patterns under certain conditions. In particular, the co-variation between VOC concentrations and the CV of O_3 reflects the influence of local precursor emissions and short-term chemical regimes, including nighttime titration by NO emissions and transient imbalances in photochemical production. This demonstrates that, despite its predominantly regional nature, the variability of O_3 can be locally amplified when chemical and emission conditions vary across urban areas. Compared with primary pollutants such as NO_2, which are dominated by short-lived local emissions, the variability of O_3 reflects a multi-scale interaction between regional background formation and local chemical modulation. This distinction is critical for interpreting CV as an indicator of emission–transport dynamics, as it shows that CV does not simply reflect spatial heterogeneity, but also encodes pollutant-specific chemical and transport characteristics. Therefore, the observed behavior of O_3 provides important evidence that the CV–RC relationship is fundamentally constrained by pollutant lifetime and formation mechanisms, rather than being a purely statistical association.

Three typical $PM_{2.5}$ pollution episodes in January 2022 were analyzed to examine the relationship between CV, concentration, and regional contribution ratio (Figure 8). Compared with O_3, $PM_{2.5}$ is less affected by rapid chemical processes and therefore provides a more stable basis for examining the relationship between concentration variability and emission–transport dynamics. In Episode I (3–4 January), CV was positively correlated with concentration before the pollution peak ($R = 0.84$), when regional contribution was relatively low. During and after the peak, CV showed a strong negative correlation with concentration ($R = -0.83$), coinciding with increased regional contribution. In Episode II (18–19 January), CV was negatively correlated with concentration throughout the event ($R = -0.65$ to -0.84), consistent with sustained dominance of regional transport. In Episode III (25–26 January), CV and concentration were positively correlated before the peak ($R = 0.76$), but became negatively correlated during and after the peak ($R = -0.59$), as regional influence increased.

Across the three $PM_{2.5}$ episodes, the observed shift from positive to negative correlation between CV and concentration reflects a transition from locally dominated conditions to regional transport dominance. Unlike O_3, $PM_{2.5}$ represents a mixed pollutant, with both primary emissions and secondary formation contributing to its concentration, and with an atmospheric lifetime longer than NO_2 but shorter than typical regional-scale O_3 transport. Previous studies have shown that particulate matter variability is strongly influenced by accumulation processes and regional transport under stagnant conditions, leading to increased spatial homogeneity during pollution episodes [38]. While these studies primarily

describe the qualitative transition from local accumulation to regional homogenization, they do not explicitly quantify how spatial variability responds to such shifts.

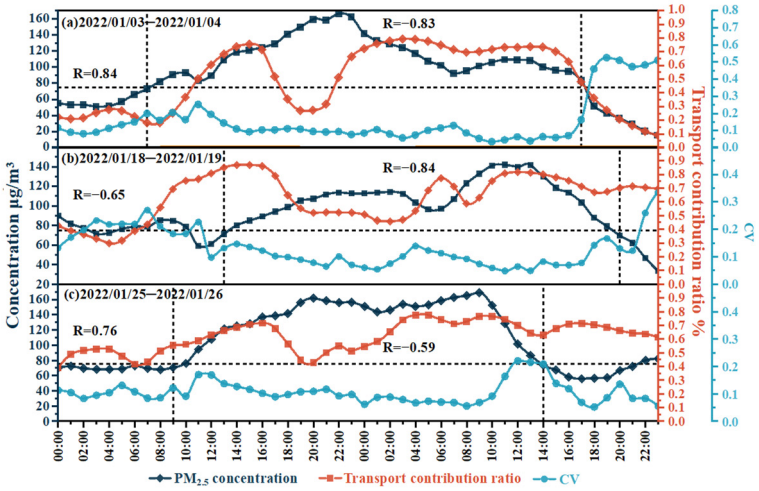

Figure 8. Hourly variation of $PM_{2.5}$ concentration, inter-station CV, and regional contribution ratio during three typical pollution episodes within the 10 km domain in Linyi in 2022. The horizontal dashed line represents the national secondary $PM_{2.5}$ standard (75 μg/m^3), while the vertical dashed lines are used to distinguish different pollution periods.

The present results extend these findings by demonstrating that such transitions can be quantitatively captured through inter-station CV. When local emissions dominate, heterogeneous source distributions lead to increasing CV with concentration. In contrast, under strong regional transport and accumulation, enhanced mixing reduces spatial gradients, resulting in decreasing CV with increasing concentration. This behavior confirms that CV responds systematically to the balance between local emission heterogeneity and regional transport, and that this response is modulated by pollutant lifetime and formation processes.

Compared with NO_2, which responds rapidly to local emissions due to its short lifetime, and O_3, which is largely controlled by regional photochemistry, $PM_{2.5}$ exhibits intermediate behavior, reflecting its mixed origin and multi-scale transport characteristics. This intermediate response further supports the interpretation that CV can serve as a unified indicator linking pollutant specific properties to emission transport dynamics, thereby providing a physically consistent basis for the CV–RC mapping framework.

Taken together, the analyses in Section 3.2 demonstrate that inter-station CV responds systematically to variations in pollution level, meteorological conditions, and emission–transport regimes, and that this response is strongly modulated by pollutant-specific properties. In particular, the contrasting behaviors of NO_2, O_3, and PM highlight the role of atmospheric lifetime and formation mechanisms in shaping spatial variability. Short-lived primary pollutants such as NO_2 exhibit strong sensitivity to local emission heterogeneity, whereas secondary pollutants such as O_3 are dominated by regional-scale processes and display more spatially coherent patterns. Particulate matter lies between these extremes, reflecting its mixed origin and intermediate lifetime.

This pollutant-dependent behavior provides a unifying physical framework for interpreting CV as more than a statistical measure of variability. Instead, CV can be understood as an emergent indicator of the relative importance of local emissions and regional transport, constrained by chemical lifetime and atmospheric processes. Compared with previous studies that describe spatial variability qualitatively, the present analysis demonstrates that CV responds in a consistent and physically interpretable manner across multiple pollu-

tants and conditions. This mechanistic consistency provides the theoretical foundation for constructing a scale-dependent and quantitative CV–RC relationship, thereby supporting its use as a rapid diagnostic tool for assessing emission–transport dominance in urban air quality systems.

3.3. Scale-Dependent Characteristics and Stability Range of the CV–RC Relationship

Based on the physical interpretation presented in Section 3.2, this section establishes the statistical relationship between inter-station CV and RC. The dependence of this relationship on temporal and spatial scales is systematically evaluated. To ensure comparability across pollution levels, concentration stratification was applied at hourly and daily scales (Table S3). Monthly data were stratified using 1 $\mu g/m^3$ intervals.

3.3.1. Influence of Temporal Scale

The CV–RC relationship was constructed at monthly, daily, and hourly scales using 2022 observations within the 10 km domain in Linyi. At the monthly scale, each data point represents one month in 2022. Due to data completeness requirements, months with missing model-simulated or observational values were excluded. As a result, ten months with valid paired CV and RC data were used for the monthly scale fitting. At the daily scale, each point corresponds to one day in 2022, and at the hourly scale, each point represents one hourly observation. All available time steps with valid paired CV and RC values are included, rather than randomly selected samples. The total number of data points at each temporal scale is therefore determined by data completeness after quality control, which may lead to differences in sample size across pollutants and temporal resolutions. The fitting curves are shown in Figure 9, and the coefficients of determination are summarized in Table 3.

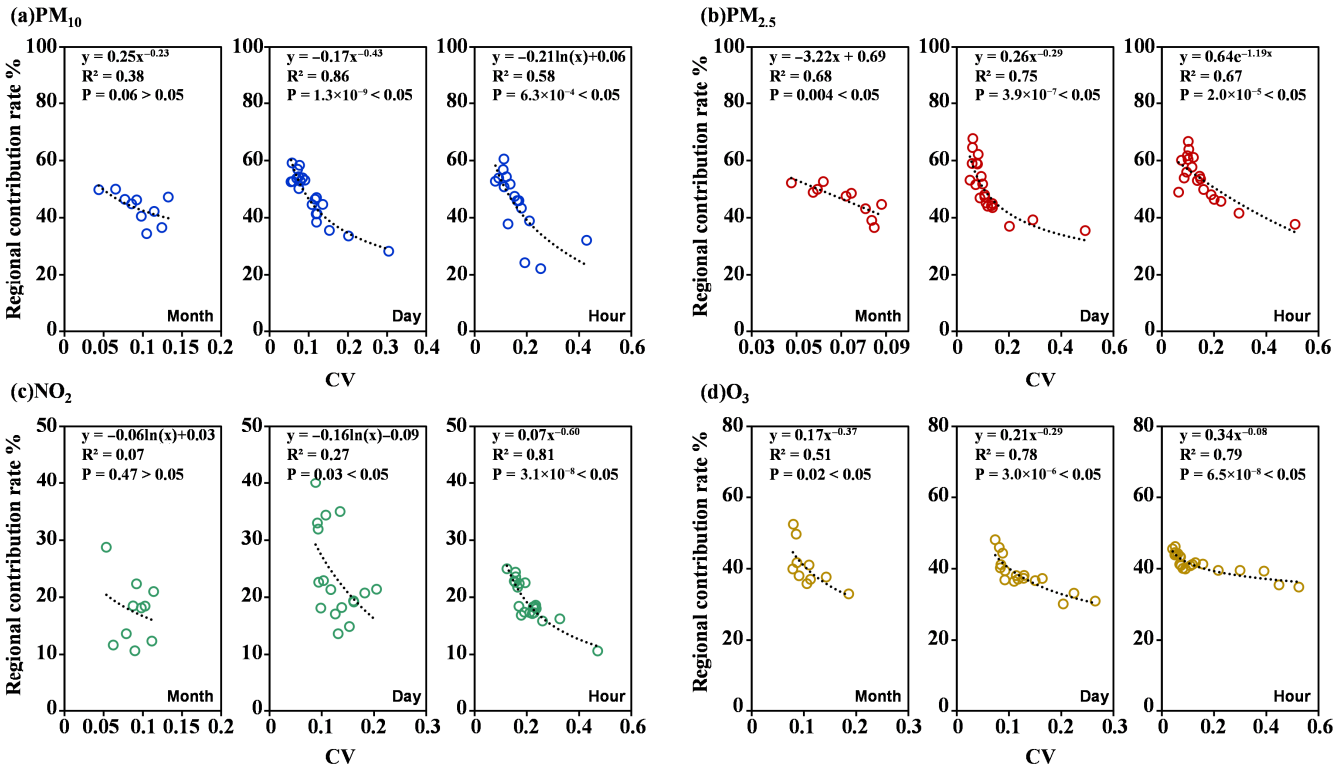

Figure 9. Fitted relationships between CV and regional contribution ratio (RC) for typical pollutants in Linyi in 2022 at different temporal scales: (**a**) PM_{10}, (**b**) $PM_{2.5}$, (**c**) NO_2, (**d**) O_3. The dashed lines represent the fitted regression relationships between CV and RC.

Table 3. Coefficient of determination for the CV–RC relationship at different temporal scales in Linyi.

R^2	Month	Day	Hour
PM_{10}	0.38	0.86	0.58
$PM_{2.5}$	0.68	0.75	0.67
O_3	0.51	0.78	0.79
NO_2	0.07	0.27	0.81

Clear differences were observed among pollutants. For PM_{10}, the strongest relationship occurred at the daily scale (R^2 = 0.86). The hourly scale showed a moderate fit (R^2 = 0.58). The monthly scale produced a weak and statistically insignificant relationship (R^2 = 0.38, $p > 0.05$). For $PM_{2.5}$, the best performance was also obtained at the daily scale (R^2 = 0.75). The hourly and monthly scales yielded slightly lower but statistically significant fits (R^2 = 0.67–0.68). For NO_2, the relationship was strongest at the hourly scale (R^2 = 0.81). The fit decreased substantially at the daily scale (R^2 = 0.27) and became negligible at the monthly scale (R^2 = 0.07). For O_3, both hourly and daily scales showed stable and strong relationships (R^2 = 0.79 and 0.78). The monthly scale produced a lower but still significant fit (R^2 = 0.51).

These results indicate that the optimal temporal scale differs among pollutants. NO_2 is best represented at the hourly scale, while PM_{10} and $PM_{2.5}$ are better resolved at the daily scale. The CV–RC relationship for O_3 maintains stable performance at both hourly and daily scales. This behavior can be explained by pollutant-specific characteristics. O_3, as a secondary pollutant with longer effective lifetime and regional-scale photochemical production, exhibits stable relationships at both hourly and daily scales, while particulate matter shows intermediate scale dependence due to its mixed primary and secondary origins. In contrast, the monthly scale relationship is weaker, which may be partly influenced by the limited number of valid monthly samples after data filtering. Excessive temporal averaging reduces the dynamic contrast between local and regional dominance and weakens statistical coupling. At the optimal temporal scale for each pollutant, the CV–RC relationship follows a power-law form, indicating a nonlinear response of RC to spatial variability.

The scale dependence of the CV–RC relationship reflects the characteristic timescales of emission, chemical transformation, and atmospheric transport processes for different pollutants. Previous studies have shown that the effectiveness of statistical relationships in air quality analysis strongly depends on whether the temporal resolution captures the dominant physical processes [27,38]. For short-lived primary pollutants such as NO_2, whose atmospheric lifetime is on the order of hours, variability is closely linked to rapidly changing local emissions and boundary-layer dynamics, making the hourly scale most appropriate. In contrast, particulate matter ($PM_{2.5}$ and PM_{10}), which is influenced by both local emissions and regional accumulation processes, exhibits stronger coupling at the daily scale where short-term fluctuations are smoothed but transport-driven variability is retained.

Compared with these established understandings, the present results provide quantitative evidence that the CV–RC relationship is optimized when the temporal resolution matches the effective lifetime and transport scale of the pollutant. The weakening of the relationship at the monthly scale further demonstrates that excessive temporal averaging suppresses the contrast between local and regional dominance, reducing the ability of CV to resolve emission–transport interactions. This finding extends previous qualitative analyses by explicitly linking temporal scale selection to the stability of a quantitative CV–RC mapping.

3.3.2. Influence of Spatial Scale

After determining the optimal temporal scale for each pollutant, the CV–RC relationship was evaluated across spatial buffer radii of 10, 15, 20, 25, 30, and 40 km. The fitting curves are shown in Figure 10. The variation of R^2 with spatial radius is summarized in Figure 11 to illustrate the overall trend of statistical strength across spatial scales.

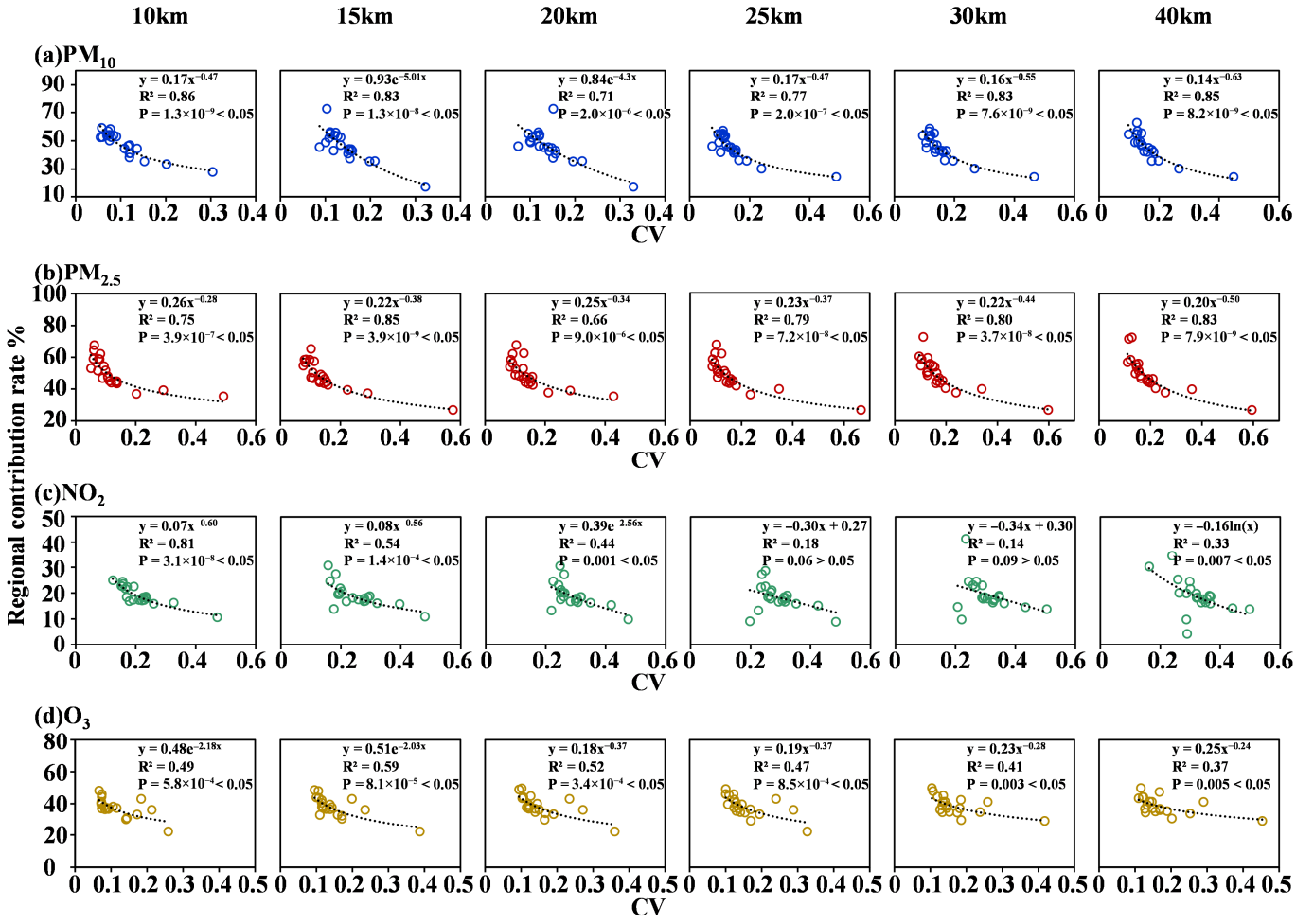

Figure 10. Fitted relationships between CV and regional contribution ratio (RC) for typical pollutants in Linyi in 2022 under different spatial scales: (**a**) PM_{10}, (**b**) $PM_{2.5}$, (**c**) NO_2, (**d**) O_3. The dashed lines represent the fitted regression relationships between CV and RC.

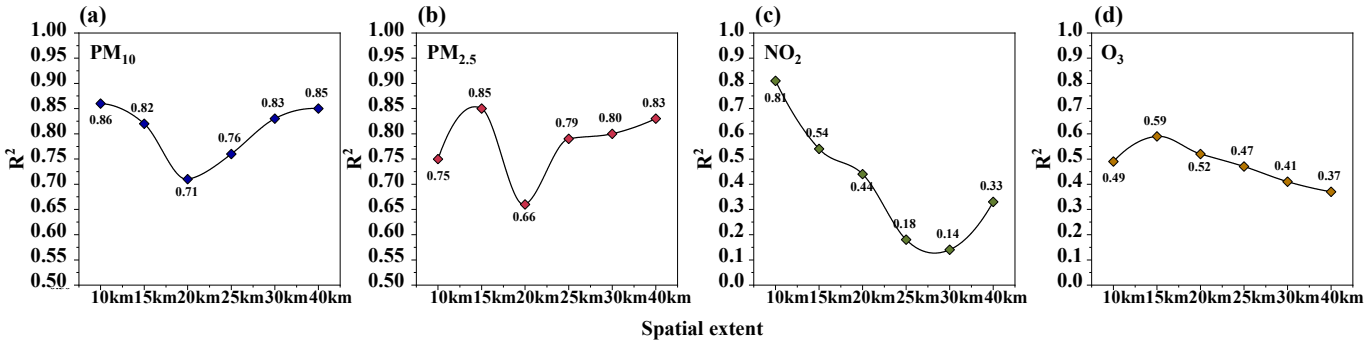

Figure 11. Variation in the coefficient of determination (R^2) for the CV–RC fitting with spatial range for typical pollutants in Linyi in 2022: (**a**) PM_{10}, (**b**) $PM_{2.5}$, (**c**) NO_2, (**d**) O_3.

For PM_{10}, the strongest fit occurred at 10 km (R^2 = 0.86). Although R^2 decreased at 20 km (0.71), the relationship remained statistically significant across 15–40 km, with R^2

values between 0.71 and 0.85. This indicates relatively stable behavior from local to urban scales. For $PM_{2.5}$, the optimal spatial scale was 15 km (R^2 = 0.85). At other radii, R^2 ranged from 0.66 to 0.83, and all fits were statistically significant. This suggests moderate sensitivity to spatial scale but overall structural stability. For O_3, the highest R^2 was observed at 15 km (0.59). The value decreased gradually as the spatial radius increased, from 0.49 at 10 km to 0.37 at 40 km. This pattern indicates that intermediate spatial scales best preserve the statistical coupling between CV and RC. For NO_2, the spatial dependence was more pronounced. The relationship was strongest at 10 km (R^2 = 0.81). R^2 decreased to 0.54 at 15 km and to 0.44 at 20 km. At 25–30 km, the relationship was no longer statistically significant ($p > 0.05$). This may be influenced by a limited number of data points and the presence of outliers, and should therefore be interpreted with caution. Although R^2 increased slightly at 40 km (0.33), the overall fit remained substantially weaker than at smaller radii. This behavior reflects the strong local dominance of NO_2. The variation of R^2 with spatial scale reflects the combined influence of spatial representativeness and station coverage. As the buffer radius increases, additional monitoring stations with more heterogeneous emission and environmental conditions are included (Figure 2), which may weaken the statistical coupling between CV and RC.

Overall, the CV–RC relationship is most stable within a spatial radius of 10–15 km, where the balance between spatial representativeness and local emission contrast is best preserved. Beyond this range, spatial averaging and the inclusion of additional stations reduce local emission gradients and weaken the statistical coupling. This trend is reflected in Figure 11 and should be interpreted together with the fitted relationships (Figure 10) and the spatial distribution of monitoring stations (Figure 2).

This scale-dependent behavior can be interpreted in the context of spatial representativeness and pollutant transport scales. Previous studies have shown that the representativeness of monitoring networks depends strongly on spatial scale, with small domains capturing local heterogeneity and larger domains increasingly reflecting regional background conditions [30,37]. In this study, the optimal range of 10–15 km represents a balance between these two regimes. At smaller scales, limited station coverage may not fully capture spatial variability, while at larger scales, the inclusion of stations influenced by different source regions and transport pathways reduces the contrast between local and regional contributions.

The stronger spatial sensitivity observed for NO_2 further reflects its short atmospheric lifetime and strong dependence on localized emission sources, whereas the more stable behavior of $PM_{2.5}$ and PM_{10} is consistent with their longer lifetimes and greater susceptibility to regional transport and accumulation. Compared with previous studies that primarily assess spatial representativeness qualitatively, the present results demonstrate that spatial scale directly affects the strength of a quantitative CV–RC relationship, thereby providing a practical basis for selecting appropriate analysis domains in observation-based source diagnostics.

3.3.3. Functional Form and Structural Stability

For all statistically significant temporal–spatial configurations, the CV–RC relationship is well described by a power-law function. This consistent functional form indicates that the response of regional contribution to spatial variability is nonlinear. At low CV values, small changes in spatial variability correspond to relatively large changes in RC. As CV increases, the marginal sensitivity of RC decreases. This pattern suggests a gradual transition from regional dominance to local dominance.

The stability of this nonlinear structure depends on appropriate temporal and spatial resolution. Monthly averaging and spatial radii larger than 15–20 km reduce statistical

coupling and weaken the robustness of the mapping. In contrast, when the analysis is conducted at the optimal temporal scale and within a spatial radius of 10–15 km, the power-law structure remains statistically significant and stable for all pollutants.

The persistence of a power-law structure across pollutants and temporal–spatial configurations indicates that the CV–RC relationship reflects a fundamental property of atmospheric transport and mixing processes rather than a case-specific empirical fit. Similar nonlinear scaling behavior has been reported in geophysical systems, where system responses exhibit diminishing sensitivity as forcing increases [48,49]. In the context of urban air pollution, this behavior can be interpreted as a transition from regionally dominated regimes, characterized by spatially homogeneous concentration fields, to locally dominated regimes with strong heterogeneity driven by emission contrasts.

Importantly, the emergence of this nonlinear relationship across pollutants with different lifetimes suggests that the CV–RC linkage is constrained by underlying physical processes rather than being pollutant-specific. Short-lived species such as NO_2 respond rapidly to local emissions, while longer-lived pollutants such as O_3 are governed by regional-scale processes, with particulate matter exhibiting intermediate behavior. The consistent power-law form across these regimes indicates that CV effectively integrates these differences into a unified statistical framework

Compared with previous studies that describe spatial variability qualitatively or through correlation-based metrics, the present analysis demonstrates that inter-station CV can be directly linked to regional contribution through a stable and scale-dependent functional relationship. This structural robustness provides a theoretical basis for using CV as a quantitative diagnostic tool and defines the operational conditions under which such mapping remains reliable. The identified stability range therefore represents not only an empirical finding, but also a physically interpretable window within which emission–transport interactions can be consistently resolved.

3.4. Application-Based Robustness Assessment

The established CV–RC mapping was applied to January 2022 data in Linyi using the optimal temporal–spatial configurations identified in Section 3.3. This assessment serves as an application-based demonstration of the CV–RC framework under realistic pollution conditions within the same annual dataset, rather than a comprehensive or independent out-of-sample validation and therefore does not represent a formal train–test separation.

January 2022 was selected as a representative period due to the presence of typical pollution episodes with clear transitions between local emission dominance and regional transport influence. This provides a suitable scenario to illustrate the applicability of the framework under dynamically varying conditions. It should be emphasized that the generality of the CV–RC relationship is not solely supported by this single-month application. Instead, it is primarily established based on the full time-series analysis across pollutants, temporal scales, and spatial domains presented in Sections 3.2 and 3.3. The January case is therefore intended as a practical example to demonstrate how the framework can be applied, rather than as independent evidence of its overall validity.

Estimated regional contributions were compared with model-simulated values (Table 4). Correlation coefficients ranged from 0.55 to 0.65. $PM_{2.5}$ showed the highest agreement (R = 0.65), followed by PM_{10} (R = 0.60) and O_3 (R = 0.57). NO_2 exhibited slightly lower consistency (R = 0.55). Bias indicators were generally moderate. $PM_{2.5}$ showed minimal bias (MB = 0.01; NMB = 0.03; NME = 0.18). PM_{10} and O_3 presented moderate deviations. NO_2 displayed larger normalized errors (NMB = 0.48; NME = 0.60), consistent with its stronger local variability.

Table 4. Performance statistics of CV-based regional contribution estimation in January 2022.

Pollutant	R	MB	NMB	NME
$PM_{2.5}$	0.65	0.01	0.03	0.18
PM_{10}	0.60	0.06	0.11	0.20
O_3	0.57	0.04	0.12	0.18
NO_2	0.55	0.07	0.48	0.60

The estimated regional contribution reproduced the same phase transitions between local-dominant and regional-dominant conditions as the simulated results during pollution evolution. Since the evaluation uses data from the same annual dataset as model construction, it represents an internal robustness assessment rather than a strict out-of-sample validation. Within the identified temporal–spatial stability range, the CV-based framework provides an interpretable, first-order estimate of urban-scale contribution patterns. Although this represents an internal robustness test rather than strict independent validation, the results confirm that CV-based inference can reproduce dominant phase transitions between local and regional control states under realistic pollution conditions.

The applicability of this framework depends on sufficient spatial coverage of monitoring stations and on the presence of mixed local and regional influences. In extremely localized source environments or in domains lacking spatial representativeness, the mapping stability may weaken. Therefore, careful scale selection remains essential for practical application.

While the present study demonstrates internal robustness within the same annual dataset, cross-year and cross-region validation is needed to further examine long-term transferability. In addition, the framework does not explicitly resolve chemical nonlinearity or secondary formation pathways, which may influence contribution estimation under extreme pollution conditions. These aspects warrant further investigation.

The application-based evaluation shows that the CV-derived estimates reproduce the temporal evolution of regional contribution with moderate but consistent agreement (R = 0.55–0.65), indicating that the proposed framework captures the dominant transitions between local emission influence and regional transport. Compared with source-oriented chemical transport models, the CV-based approach provides a simplified, observation-driven diagnostic based on spatial variability rather than explicit process simulation, which explains the observed deviations. In addition, it should be noted that biases in the WRF–CAMx simulations relative to observations (Table 2) may propagate into the derived CV–RC relationship, introducing both systematic shifts and additional scatter in the fitted relationship.

The performance differences among pollutants can be interpreted in the context of their chemical and transport characteristics. NO_2 shows weaker agreement due to its short atmospheric lifetime and strong sensitivity to local emission heterogeneity, which limits the ability of spatial variability alone to represent regional contribution. In contrast, $PM_{2.5}$ exhibits higher consistency, reflecting its longer lifetime and stronger influence from regional transport and accumulation processes. O_3 shows intermediate performance, as its variability is primarily controlled by regional photochemical production but can be modulated by local precursor emissions and titration effects. These patterns are consistent with previous studies showing that regional transport and secondary formation processes enhance spatial coherence in urban pollution fields [7,38].

Compared with existing source apportionment approaches, which rely on detailed emission inventories and chemical transport modeling, the CV-based framework provides an observation-driven diagnostic that uses spatial variability as a proxy for emission–transport balance [50,51]. While previous studies have described the influence of local

emissions and regional transport on spatial variability qualitatively, the present study demonstrates that inter-station CV can be quantitatively linked to regional contribution through a stable and scale-dependent functional relationship. This provides a new observational pathway for diagnosing local–regional contribution balance without relying on detailed emission inventories or full chemical transport simulations.

Several limitations should be noted. The analysis is based on internal consistency within the same dataset, and the use of a 2020 emission inventory introduces structural uncertainty in the reference values. In addition, nonlinear chemical processes, particularly for secondary pollutants, are not explicitly resolved. Despite these limitations, the results indicate that CV captures the essential structure of emission–transport interactions and provides a physically interpretable and computationally efficient indicator of regional contribution within the identified temporal–spatial stability range.

4. Conclusions

This study establishes a scale-dependent relationship between inter-station CV and RC across multiple pollutants based on observational and model-simulated data. The results indicate that CV contains physically meaningful information on the balance between local emissions and regional transport, with lower variability associated with stronger regional influence and higher variability reflecting enhanced local emission heterogeneity. This represents a shift from descriptive analysis of spatial variability to a quantitative and physically interpretable framework for linking observations to source contribution.

However, this relationship is bounded. It is most reliable within a defined temporal–spatial window, particularly at pollutant-specific temporal scales and within spatial radii of approximately 10–15 km. Outside these ranges, the coupling between variability and contribution weakens, reducing interpretability.

Inter-station variability can therefore be interpreted as an emergent indicator of emission–transport balance under appropriate conditions. In addition, its response to meteorological factors such as wind speed is pollutant-dependent, with primary pollutants maintaining spatial contrasts and secondary pollutants such as O_3 tending toward increased spatial homogenization under stronger wind conditions. At the same time, the framework has limitations. It is less effective for pollutants with short atmospheric lifetimes and strong local emission dominance (e.g., NO_2), which tend to exhibit pronounced spatial heterogeneity, or for pollutants governed by nonlinear chemistry and regional-scale photochemical production (e.g., O_3), whose spatial variability reflects multi-scale processes. Particulate matter exhibits intermediate behavior due to its mixed primary and secondary origins. In addition, its performance may be affected by meteorological variability, emission inventory uncertainty, and potential biases in model-derived regional contribution, which may propagate into the CV–RC relationship.

It should also be noted that the present evaluation is based on internal consistency within the same dataset rather than strict out-of-sample validation. Therefore, the framework should be interpreted as a first-order diagnostic tool.

Overall, the proposed CV-based framework provides a computationally efficient, observation-driven diagnostic that bridges the gap between purely statistical variability analysis and process-based source apportionment methods. Future work should focus on cross-year and cross-city validation to further assess its generalizability.

Supplementary Materials: The following supporting information can be downloaded at: https://www.mdpi.com/article/10.3390/atmos17050481/s1, Table S1. Seasonal mean concentrations of PM_{10}, $PM_{2.5}$, NO_2, and O_3 for representative months (January, April, July, and October) during 2019–2022 within the 25 km urban domain of central Linyi. Table S2. Diurnal mean concentrations of PM_{10}, $PM_{2.5}$, NO_2, and O_3 during 2019–2022 within the 25 km urban domain of central Linyi.

Table S3. Classification of hourly and daily concentration ranges for typical pollutants ($\mu g/m^{-3}$). Figure S1. Monthly variation in inter-station concentration CV for PM_{10}, $PM_{2.5}$, NO_2, and O_3 in Linyi from 2018 to 2022. Figure S2. Concentration-stratified distributions of the coefficient of variation (CV) at the hourly scale in Linyi for PM_{10}, $PM_{2.5}$, NO_2, and O_3. Figure S3. Wind-direction dependence of concentration CV among monitoring stations in 2022: (a) CV values for PM_{10}, $PM_{2.5}$, NO_2, and O_3 under different wind direction in Linyi, Xi'an, and Beijing; (b) wind rose diagrams for the three cities in 2022. Figure S4. Wind-speed-stratified distributions of the coefficient of variation (CV) among monitoring stations for individual pollutants (PM_{10}, $PM_{2.5}$, NO_2, and O_3) in Linyi in 2022.

Author Contributions: Conceptualization, Y.W. (Yixuan Wang) and X.Y.; methodology, J.L. (Jianlei Lang); software, Y.W. (Yixuan Wang) and X.Y.; investigation, Y.W. (Yadong Wang); resources, J.L. (Jianlei Lang) and Y.Z.; writing—original draft preparation, Y.W. (Yixuan Wang), J.L. (Jianghui Liu) and X.Y.; writing—review and editing, Y.W. (Yixuan Wang) and J.L. (Jianlei Lang); visualization, Q.M.; funding acquisition, J.L. (Jianlei Lang). All authors have read and agreed to the published version of the manuscript.

Funding: This research was funded by Beijing Nova Program (20250484979), Jing-Jin-Ji Regional Integrated Environmental Improvement-National Science and Technology Major Project (2024ZD1200202).

Institutional Review Board Statement: Not applicable.

Informed Consent Statement: Not applicable.

Data Availability Statement: The data presented in this study are available on request from the corresponding author due to privacy.

Acknowledgments: The authors are grateful to the anonymous reviewers for their insightful comments.

Conflicts of Interest: The authors declare no conflicts of interest.

References

1. Fuller, R.; Landrigan, P.J.; Balakrishnan, K.; Bathan, G.; Bose-O'Reilly, S.; Brauer, M.; Caravanos, J.; Chiles, T.; Cohen, A.; Corra, L.; et al. Pollution and Health: A Progress Update. *Lancet Planet. Health* **2022**, *6*, e535–e547. [CrossRef]
2. Southerland, V.A.; Brauer, M.; Mohegh, A.; Hammer, M.S.; van Donkelaar, A.; Martin, R.V.; Apte, J.S.; Anenberg, S.C. Global Urban Temporal Trends in Fine Particulate Matter ($PM_{2.5}$) and Attributable Health Burdens: Estimates from Global Datasets. *Lancet Planet. Health* **2022**, *6*, e139–e146. [CrossRef]
3. Kilpatrick, D.J.; Hung, P.Y.; Crouch, E.; Self, S.; Cothran, J.; Porter, D.E.; Eberth, J.M. Geographic Variations in Urban-Rural Particulate Matter ($PM_{2.5}$) Concentrations in the United States, 2010–2019. *GeoHealth* **2024**, *8*, e2023GH000920. [CrossRef]
4. Huang, R.-J.; Zhang, Y.L.; Bozzetti, C.; Ho, K.-F.; Cao, J.-J.; Han, Y.M.; Daellenbach, K.R.; Slowik, J.G.; Platt, S.M.; Canonaco, F.; et al. High Secondary Aerosol Contribution to Particulate Pollution During Haze Events in China. *Nature* **2014**, *514*, 218–222. [CrossRef]
5. Zheng, G.J.; Duan, F.K.; Su, H.; Ma, Y.L.; Cheng, Y.; Zheng, B.; Zhang, Q.; Huang, T.; Kimoto, T.; Chang, D.; et al. Exploring the Severe Winter Haze in Beijing: The Impact of Synoptic Weather, Regional Transport and Heterogeneous Reactions. *Atmos. Chem. Phys.* **2015**, *15*, 2969–2983. [CrossRef]
6. Zhan, Y.Z.H.; Xie, M.; Zhao, W.; Wang, T.J.; Gao, D.; Chen, P.L.; Tian, J.; Zhu, K.G.; Li, S.; Zhuang, B.L.; et al. Quantifying the Seasonal Variations in and Regional Transport of Pm2.5 in the Yangtze River Delta Region, China: Characteristics, Sources, and Health Risks. *Atmos. Chem. Phys.* **2023**, *23*, 9837–9852. [CrossRef]
7. An, Z.S.; Huang, R.-J.; Zhang, R.Y.; Tie, X.X.; Li, G.H.; Cao, J.J.; Zhou, W.J.; Shi, Z.G.; Han, Y.M.; Gu, Z.L.; et al. Severe Haze in Northern China: A Synergy of Anthropogenic Emissions and Atmospheric Processes. *Proc. Natl. Acad. Sci. USA* **2019**, *116*, 8657–8666. [CrossRef] [PubMed]
8. Cai, S.Y.; Wang, Y.J.; Zhao, B.; Wang, S.X.; Chang, X.; Hao, J.M. The Impact of the "Air Pollution Prevention and Control Action Plan" on $PM_{2.5}$ Concentrations in Jing-Jin-Ji Region During 2012–2020. *Sci. Total Environ.* **2017**, *580*, 197–209. [CrossRef] [PubMed]
9. Sokhi, R.S.; Moussiopoulos, N.; Baklanov, A.; Bartzis, J.; Coll, I.; Finardi, S.; Friedrich, R.; Geels, C.; Grönholm, T.; Halenka, T.; et al. Advances in Air Quality Research—Current and Emerging Challenges. *Atmos. Chem. Phys.* **2022**, *22*, 4615–4703. [CrossRef]
10. Jiang, S.N.; Kong, S.F.; Zheng, H.; Wu, J.; Yao, L.Q.; Chen, N.; Zhu, B.; Zhao, T.L.; Bai, Y.Q.; Liu, D.T.; et al. Winter-Autumn Air Pollution Control Plan in North China Modified the $PM_{2.5}$ Compositions and Sources in Central China. *Atmos. Environ.* **2023**, *306*, 119827. [CrossRef]

11. Gao, Z.Q.; Zhou, X.H. A Review of the Camx, Cmaq, Wrf-Chem and Naqpms Models: Application, Evaluation and Uncertainty Factors. *Environ. Pollut.* **2024**, *343*, 123183. [CrossRef]
12. Karamchandani, P.; Long, Y.; Pirovano, G.; Balzarini, A.; Yarwood, G. Source-Sector Contributions to European Ozone and Fine Pm in 2010 Using Aqmeii Modeling Data. *Atmos. Chem. Phys.* **2017**, *17*, 5643–5664. [CrossRef]
13. Byun, D.; Schere, K.L. Review of the Governing Equations, Computational Algorithms, and Other Components of the Models-3 Community Multiscale Air Quality (Cmaq) Modeling System. *Appl. Mech. Rev.* **2006**, *59*, 51–77. [CrossRef]
14. Appel, K.W.; Napelenok, S.L.; Foley, K.M.; Pye, H.O.T.; Hogrefe, C.; Luecken, D.J.; Bash, J.O.; Roselle, S.J.; Pleim, J.E.; Foroutan, H.; et al. Description and Evaluation of the Community Multiscale Air Quality (Cmaq) Modeling System Version 5.1. *Geosci. Model Dev.* **2017**, *10*, 1703–1732. [CrossRef] [PubMed]
15. Grell, G.A.; Peckham, S.E.; Schmitz, R.; McKeen, S.A.; Frost, G.; Skamarock, W.C.; Eder, B. Fully Coupled "Online" Chemistry within the Wrf Model. *Atmos. Environ.* **2005**, *39*, 6957–6975. [CrossRef]
16. Ye, X.P.; Yang, J.; Chen, Z.W.; Liu, G.; Sun, J.; Jiang, Q.; Huang, X.; Gao, Y.; Niu, X.Y.; Xu, H.M.; et al. Triangulating Residential Biomass Burning Impacts on $PM_{2.5}$ Via Pmf, Satellite Observation-Based Emission Inventory, and Wrf-Chem. *Environ. Int.* **2025**, *201*, 109580. [CrossRef] [PubMed]
17. Hanna, S.R.; Lu, Z.G.; Frey, H.C.; Wheeler, N.; Vukovich, J.; Arunachalam, S.; Fernau, M.; Hansen, D.A. Uncertainties in Predicted Ozone Concentrations Due to Input Uncertainties for the Uam-V Photochemical Grid Model Applied to the July 1995 Otag Domain. *Atmos. Environ.* **2001**, *35*, 891–903. [CrossRef]
18. Bond, T.C.; Streets, D.G.; Yarber, K.F.; Nelson, S.M.; Woo, J.-H.; Klimont, Z. A Technology-Based Global Inventory of Black and Organic Carbon Emissions from Combustion. *J. Geophys. Res. Atmos.* **2004**, *109*, 1–43. [CrossRef]
19. Sarkar, M.; Venkataraman, C.; Guttikunda, S.; Sadavarte, P. Indian Emissions of Technology-Linked Nmvocs with Chemical Speciation: An Evaluation of the Saprc99 Mechanism with Wrf-Camx Simulations. *Atmos. Environ.* **2016**, *134*, 70–83. [CrossRef]
20. Yu, S.C.; Mathur, R.; Schere, K.; Kang, D.W.; Pleim, J.; Otte, T.L. A Detailed Evaluation of the Eta-Cmaq Forecast Model Performance for O_3, Its Related Precursors, and Meteorological Parameters During the 2004 Icartt Study. *J. Geophys. Res. Atmos.* **2007**, *112*, 1–24. [CrossRef]
21. Baklanov, A.; Schlünzen, K.; Suppan, P.; Baldasano, J.; Brunner, D.; Aksoyoglu, S.; Carmichael, G.; Douros, J.; Flemming, J.; Forkel, R.; et al. Online Coupled Regional Meteorology Chemistry Models in Europe: Current Status and Prospects. *Atmos. Chem. Phys.* **2014**, *14*, 317–398. [CrossRef]
22. Luo, Z.W.; Han, Y.; Hua, K.; Zhang, Y.F.; Wu, J.H.; Bi, X.H.; Dai, Q.L.; Liu, B.S.; Chen, Y.; Long, X.; et al. The Effect of Emission Source Chemical Profiles on Simulated $PM_{2.5}$ Components: Sensitivity Analysis with the Community Multiscale Air Quality (Cmaq) Modeling System Version 5.0.2. *Geosci. Model Dev.* **2023**, *16*, 6757–6771. [CrossRef]
23. Hopke, P.K. Review of Receptor Modeling Methods for Source Apportionment. *J. Air Waste Manag. Assoc.* **2016**, *66*, 237–259. [CrossRef]
24. Huang, H.Y.; Liu, B.S.; Li, S.; Choe, T.-H.; Dai, Q.L.; Gu, Y.; Diao, L.L.; Zhang, S.F.; Bi, X.H.; Luo, Z.W.; et al. An Estimation Method for Regional Transport Contributions from Emission Sources Based on a High-Mountain Site: A Case Study in Zhumadian, China. *Atmos. Environ.* **2021**, *263*, 118664. [CrossRef]
25. Wang, Q.Q.; Zhu, S.H.; Wang, S.; Huang, C.; Duan, Y.S.; Yu, J.Z. Short-Term Source Apportionment of Fine Particulate Matter with Time-Dependent Profiles Using Sofi Pro: Exploring the Reliability of Rolling Positive Matrix Factorization (Pmf) Applied to Bihourly Molecular and Elemental Tracer Data. *Atmos. Chem. Phys.* **2024**, *24*, 475–486. [CrossRef]
26. Srivastava, D.; Saksakulkrai, S.; Acton, W.J.F.; Rooney, D.J.; Hall, J.; Hou, S.Q.; Wolstencroft, M.; Bartington, S.; Harrison, R.M.; Shi, Z.B.; et al. Comparative Receptor Modelling for the Sources of Fine Particulate Matter ($PM_{2.5}$) at Urban Sites in the UK. *Atmos. Environ.* **2025**, *343*, 120963. [CrossRef]
27. Tai, A.P.K.; Mickley, L.J.; Jacob, D.J. Correlations between Fine Particulate Matter ($PM_{2.5}$) and Meteorological Variables in the United States: Implications for the Sensitivity of $PM_{2.5}$ to Climate Change. *Atmos. Environ.* **2010**, *44*, 3976–3984. [CrossRef]
28. Shen, Y.; Zhang, L.P.; Fang, X.; Ji, H.Y.; Li, X.; Zhao, Z.W. Spatiotemporal Patterns of Recent $PM_{2.5}$ Concentrations over Typical Urban Agglomerations in China. *Sci. Total Environ.* **2019**, *655*, 13–26. [CrossRef]
29. Lekinwala, N.L.; Bhardwaj, A.; Raman, R.S.; Bhushan, M.; Bali, K.; Dey, S. A Framework for Setting up a Country-Wide Network of Regional Surface $PM_{2.5}$ Sampling Sites Utilising a Satellite-Derived Proxy—The Coalesce Project, India. *Atmos. Environ.* **2020**, *234*, 117544. [CrossRef]
30. Yatkin, S.; Gerboles, M.; Belis, C.A.; Karagulian, F.; Lagler, F.; Barbiere, M.; Borowiak, A. Representativeness of an Air Quality Monitoring Station for $PM_{2.5}$ and Source Apportionment over a Small Urban Domain. *Atmos. Pollut. Res.* **2020**, *11*, 225–233. [CrossRef] [PubMed]
31. Han, S.; Park, Y.; Noh, N.; Kim, J.-H.; Kim, J.-J.; Kim, B.-M.; Choi, W. Spatiotemporal Variability of the $PM_{2.5}$ Distribution and Weather Anomalies During Severe Pollution Events: Observations from 462 Air Quality Monitoring Stations across South Korea. *Atmos. Pollut. Res.* **2023**, *14*, 101676. [CrossRef]

32. Grange, S.K.; Carslaw, D.C.; Lewis, A.C.; Boleti, E.; Hueglin, C. Random Forest Meteorological Normalisation Models for Swiss PM_{10} Trend Analysis. *Atmos. Chem. Phys.* **2018**, *18*, 6223–6239. [CrossRef]
33. Reichstein, M.; Camps-Valls, G.; Stevens, B.; Jung, M.; Denzler, J.; Carvalhais, N.; Prabhat, F. Deep Learning and Process Understanding for Data-Driven Earth System Science. *Nature* **2019**, *566*, 195–204. [CrossRef] [PubMed]
34. Houdou, A.; El Badisy, I.; Khomsi, K.; Abdala, S.A.; Abdulla, F.; Najmi, H.; Obtel, M.; Belyamani, L.; Ibrahimi, A.; Khalis, M. Interpretable Machine Learning Approaches for Forecasting and Predicting Air Pollution: A Systematic Review. *Aerosol Air Qual. Res.* **2024**, *24*, 230151. [CrossRef]
35. Snyder, E.G.; Watkins, T.H.; Solomon, P.A.; Thoma, E.D.; Williams, R.W.; Hagler, G.S.W.; Shelow, D.; Hindin, D.A.; Kilaru, V.J.; Preuss, P.W. The Changing Paradigm of Air Pollution Monitoring. *Environ. Sci. Technol.* **2013**, *47*, 11369–11377. [CrossRef]
36. Harrison, R.M.; Deacon, A.R. Spatial Correlation of Automatic Air Quality Monitoring at Urban Background Sites: Implications for Network Design. *Environ. Technol.* **1998**, *19*, 121–132. [CrossRef]
37. Li, R.; Wang, J.; Xue, K.X.; Fang, C.S. Spatial and Temporal Distribution Characteristics and Influencing Factors Analysis of Particulate Matter Pollution in Jinan City. *Air Qual. Atmos. Health* **2021**, *14*, 1267–1278. [CrossRef]
38. Sun, Y.L.; Chen, C.; Zhang, Y.J.; Xu, W.Q.; Zhou, L.B.; Cheng, X.L.; Zheng, H.T.; Ji, D.S.; Li, J.; Tang, X.; et al. Rapid Formation and Evolution of an Extreme Haze Episode in Northern China During Winter 2015. *Sci. Rep.* **2016**, *6*, 27151. [CrossRef]
39. Apte, J.S.; Messier, K.P.; Gani, S.; Brauer, M.; Kirchstetter, T.W.; Lunden, M.M.; Marshall, J.D.; Portier, C.J.; Vermeulen, R.C.H.; Hamburg, S.P. High-Resolution Air Pollution Mapping with Google Street View Cars: Exploiting Big Data. *Environ. Sci. Technol.* **2017**, *51*, 6999–7008. [CrossRef]
40. Sulaymon, I.D.; Zhang, Y.X.; Hopke, P.K.; Guo, S.; Ye, F.; Sun, J.J.; Zhu, Y.; Hu, J.L. Using the COVID-19 Lockdown to Identify Atmospheric Processes and Meteorology Influences on Regional $PM_{2.5}$ Pollution Episodes in the Beijing-Tianjin-Hebei, China. *Atmos. Res.* **2023**, *294*, 106940. [CrossRef]
41. Wilson, J.G.; Kingham, S.; Pearce, J.; Sturman, A.P. A Review of Intraurban Variations in Particulate Air Pollution: Implications for Epidemiological Research. *Atmos. Environ.* **2005**, *39*, 6444–6462. [CrossRef]
42. Marshall, J.D.; Nethery, E.; Brauer, M. Within-Urban Variability in Ambient Air Pollution: Comparison of Estimation Methods. *Atmos. Environ.* **2008**, *42*, 1359–1369. [CrossRef]
43. Kim, E.; Hopke, P.K.; Pinto, J.P.; Wilson, W.E. Spatial Variability of Fine Particle Mass, Components, and Source Contributions During the Regional Air Pollution Study in St. Louis. *Environ. Sci. Technol.* **2005**, *39*, 4172–4179. [CrossRef]
44. Martuzevicius, D.; Luo, J.X.; Reponen, T.; Shukla, R.; Kelley, A.L.; Clair, H.S.; Grinshpun, S.A. Evaluation and Optimization of an Urban $PM_{2.5}$ Monitoring Network. *J. Environ. Monit.* **2005**, *7*, 67–77. [CrossRef]
45. Faridi, S.; Niazi, S.; Yousefian, F.; Azimi, F.; Pasalari, H.; Momeniha, F.; Mokammel, A.; Gholampour, A.; Hassanvand, M.S.; Naddafi, K. Spatial Homogeneity and Heterogeneity of Ambient Air Pollutants in Tehran. *Sci. Total Environ.* **2019**, *697*, 134123. [CrossRef]
46. Wu, H.; Reis, S.; Lin, C.; Beverland, I.J.; Heal, M.R. Identifying Drivers for the Intra-Urban Spatial Variability of Airborne Particulate Matter Components and Their Interrelationships. *Atmos. Environ.* **2015**, *112*, 306–316. [CrossRef]
47. Barrero, M.A.; Orza, J.A.G.; Cabello, M.; Cantón, L. Categorisation of Air Quality Monitoring Stations by Evaluation of PM_{10} Variability. *Sci. Total Environ.* **2015**, *524*, 225–236. [CrossRef]
48. Salazar, J.; Collins, L.R. Two-Particle Dispersion in Isotropic Turbulent Flows. *Annu. Rev. Fluid Mech.* **2009**, *41*, 405–432. [CrossRef]
49. Meyerjürgens, J.; Ricker, M.; Schakau, V.; Badewien, T.H.; Stanev, E.V. Relative Dispersion of Surface Drifters in the North Sea: The Effect of Tides on Mesoscale Diffusivity. *J. Geophys. Res.-Ocean.* **2020**, *125*, e2019JC015925. [CrossRef]
50. Belis, C.A.; Karagulian, F.; Larsen, B.R.; Hopke, P.K. Critical Review and Meta-Analysis of Ambient Particulate Matter Source Apportionment Using Receptor Models in Europe. *Atmos. Environ.* **2013**, *69*, 94–108. [CrossRef]
51. Thunis, P.; Clappier, A.; Tarrason, L.; Cuvelier, C.; Monteiro, A.; Pisoni, E.; Wesseling, J.; Belis, C.A.; Pirovano, G.; Janssen, S.; et al. Source Apportionment to Support Air Quality Planning: Strengths and Weaknesses of Existing Approaches. *Environ. Int.* **2019**, *130*, 104825. [CrossRef]